# Colour and Tropospheric Cloud Structure of Jupiter from MUSE/VLT: Retrieving a Universal Chromophore

Ashwin S. Braude[a,b,*], Patrick G. J. Irwin[a], Glenn S. Orton[c], Leigh N. Fletcher[d]

[a]*Department of Physics, University of Oxford, Parks Rd, Oxford, OX1 3PU, UK.*
[b]*Laboratoire Atmosphères, Milieux, Observations Spatiales (LATMOS), UVSQ Université Paris-Saclay, Sorbonne Université, CNRS, Paris, France*
[c]*Jet Propulsion Laboratory, California Institute of Technology, 4800 Oak Grove Drive, Pasadena, CA 91109, USA.*
[d]*Department of Physics & Astronomy, University of Leicester, University Road, Leicester, LE1 7RH, UK.*

## Abstract

Recent work by Sromovsky et al. (2017, Icarus 291, 232-244) suggested that all red colour in Jupiter's atmosphere could be explained by a single colour-carrying compound, a so-called 'universal chromophore'. We tested this hypothesis on ground-based spectroscopic observations in the visible and near-infrared (480-930 nm) from the VLT/MUSE instrument between 2014 and 2018, retrieving a chromophore absorption spectrum directly from the North Equatorial Belt, and applying it to model spatial variations in colour, tropospheric cloud and haze structure on Jupiter. We found that we could model both the belts and the Great Red Spot of Jupiter using the same chromophore compound, but that this chromophore must exhibit a steeper blue-absorption gradient than the proposed chromophore of Carlson et al. (2016, Icarus 274, 106–115). We retrieved this chromophore to be located no deeper than $0.2 \pm 0.1$ bars in the Great Red Spot and $0.7 \pm 0.1$ bars elsewhere on Jupiter. However, we also identified some spectral variability between 510 nm and 540 nm that could not be accounted for by a universal chromophore.

*Corresponding author
*Email address:* ashwin.braude@latmos.ipsl.fr (Ashwin S. Braude)

In addition, we retrieved a thick, global cloud layer at $1.4 \pm 0.3$ bars that was relatively spatially invariant in altitude across Jupiter. We found that this cloud layer was best characterised by a real refractive index close to that of ammonia ice in the belts and the Great Red Spot, and poorly characterised by a real refractive index of 1.6 or greater. This may be the result of ammonia cloud at higher altitude obscuring a deeper cloud layer of unknown composition.

*Keywords:* Atmospheres, composition, Jovian planets, Jupiter, Jupiter, atmosphere, Radiative transfer

---

## 1. Introduction

Spatial and temporal variation in red colour on Jupiter is thought to be due to the presence of red colour-carrying compounds ('chromophores') whose origin, composition and altitude remain unknown. A number of factors contribute to the difficulty of identifying Jovian chromophore composition. These include the apparent absence of characteristic absorption bands other than a broad absorption feature at blue wavelengths, a relative lack of laboratory studies performed under realistic Jovian conditions, and comprehensive spectral data of Jupiter at the required wavelength range and resolution. Historically, most scientific studies of colour on Jupiter have relied on a restricted number of wavelength filters (eg. Owen and Terrile, 1981; Thompson, 1990; Simon-Miller et al., 2001; Strycker et al., 2011; Ordóñez-Etxeberria et al., 2016), but various effects (such as chromophore composition, altitude and particle size) can alter the shape of Jovian spectra at short wavelengths, which can only be decoupled from each other through the observation of Jovian spectra at greater spectral resolution than filter imaging can provide. The last global sets of hyperspectral data of Jupiter in the visible wavelength range were obtained from the Cassini/VIMS-V instrument (Brown et al., 2004; Coradini et al., 2004), which observed Jupiter at wavelengths

between 350 nm and 1100 nm during its brief flyby in 2000/2001. Sromovsky et al. (2017) used these data to propose the idea of a 'universal chromophore' for Jupiter, in which all red colour on Jupiter originated from the same source compound and reaction process. This compound was based on the red substance obtained by Carlson et al. (2016) in the laboratory through the reaction of photolysed ammonia with acetylene, consisting of a range of complex organic compounds that absorb strongly at blue wavelengths due to molecular $\pi \rightarrow \pi^*$ bond transitions (Nassau, 1983). Baines et al. (2019) found that this chromophore was most likely located in a narrow layer in the upper troposphere just above the level of the ammonia clouds (the so-called *'Crème Brûlée* model'). However, elements of Jupiter's appearance have changed considerably since the Cassini flyby. We note in particular the dramatic reddening of the Great Red Spot (GRS) that has accompanied its progressive shrinking in size (Simon et al., 2014, 2018), as well as progressive cycles of colour changes in the southern North Temperate Belt (NTB) as reviewed by Rogers (1995) and Fletcher (2017). These provide additional opportunities for constraint of the origin and altitude of chromophores in Jupiter's atmosphere that were not previously available.

This paper makes use of global, hyperspectral data of Jupiter obtained at visible and near-infrared wavelengths from the ground-based VLT/MUSE instrument (described in section 2). Uniquely, these data include spectra both of the GRS in its current deep red state and of the southern NTB when it was at its reddest in early 2017. Using a radiative-transfer model (section 3), and building on the preliminary results presented in Irwin et al. (2018; 2019a), we retrieve a range of possible chromophore refractive index solutions from limb-darkening analysis of the North Equatorial Belt (NEB), given different prior particle-size distributions, and fit them to a spectrum of the GRS in order to show that a chromophore solution that is universal to all red regions of Jupiter is possible (section 4). We

then apply this chromophore solution more broadly to model spatial variations in colour and tropospheric cloud structure (section 5), showing that there is some spectral variability between 0.51 μm and 0.54 μm that cannot be explained by a universal chromophore alone. All our findings are summarised in section 6.

## 2. Data

### *2.1. Description of VLT/MUSE observations*

The Multi-Unit Spectroscopic Explorer (MUSE), mounted on the European Southern Observatory's Very Large Telescope (VLT), is an integral-field spectrograph (Bacon et al., 2010), whose spectral range nominally covers wavelengths from 480 nm to 930 nm (in practice closer to 476 to 933 nm), with radiance values sampled at 0.125 nm intervals (R~1770-3590). Even at solar opposition, Jupiter's entire visible hemisphere fits neatly into MUSE's 64" x 64" field-of-view, which is subdivided into individual 2-D spatial pixels of size 0.2" x 0.2" (subtending a great circle of approximately 640 km at nadir when Jupiter is at 5.4 AU from the Sun), each of which contain a single, invertible spectrum of Jupiter. To date, MUSE is the only instrument that can obtain data such as this within an exposure time of a fraction of a second. Its observations therefore play a crucial part in the ground support of NASA's Juno mission currently in orbit around Jupiter (although we do not include any analysis of Juno data in this paper), which has no instruments on board that can observe Jupiter at the required wavelength range (aside from JunoCam (Hansen et al., 2014), a public outreach camera with low SNR) and which has a narrow spatial footprint.

A number of sets of observations of Jupiter were obtained by the MUSE instrument between 2014 and 2018. When combined, these datasets provide a unique view of temporal changes in the visible appearance of Jupiter before and during the Juno mission that are largely beyond the scope of this paper. In order

simply to focus on the potential applicability of a universal chromophore, we instead primarily use a single observation of Jupiter in April 2018 (timestamp 2018-04-09T06:04:06.918). This observation was obtained under the best observing conditions (with seeing of just 0.38" and an airmass of close to 1) of all the datasets, and also consisted of an observation of the GRS close to nadir. For comparison, we have also included an observation from February 2014 (2014-02-17T02:07:56.907), which contained an observation of the GRS before its current, shrunken state, as well as one from May 2017 (2017-05-15T02:01:59.328) when the southern NTB was at its reddest following an upheaval in the region in the previous year (Sánchez-Lavega et al., 2017). These observations are listed in Table 1 and shown individually at sample wavelengths in Figure 1. Given our lack of knowledge of the uncertainty in the PSF, we have avoided performing retrievals close to Jupiter's terminator where the surrounding sky would have provided a non-negligible contribution to the observed spectrum. On top of these MUSE data, we also make use of a single ready-calibrated Cassini/VIMS spectrum of the GRS obtained in 2000, as provided in the supplementary material of Carlson et al. (2016), to provide broader context to temporal changes in spectra of the GRS. We do not describe the calibration procedure of this latter observation here, instead we refer the reader to Baines et al. (2019) for a more detailed explanation.

## 2.2. *Calibration and post-processing*

Calibration and reduction of each dataset was performed using the standard ESOREX pipeline (Weilbacher et al., 2014). Following calibration, the spectral image cubes were projected manually using ellipsoid limb fitting and the associated navigational metadata calculated. As described in Irwin et al. (2018), the resulting spectral image cubes were then smoothed using a triangular instrument function of FWHM = 2 nm (R~200) akin to that of the IRTF/SpeX instrument (Rayner et al., 2003), which was then sampled at 1 nm resolution. This was in

order to be compatible with the methane band data of Karkoschka and Tomasko (2010) and the reference solar spectrum (Chance and Kurucz, 2010), for which higher-resolution data is not available at the required wavelength range, as well as to save on computational time. Poor flat-fielding in the 2014-02-17T02:07:56.907 dataset resulted in visible striping artefacts which were smoothed over by convolving the data with a Gaussian filter of FWHM = 0.3 arcsecs, thereby resulting in some loss of spatial resolution compared with the other two datasets.

Spectral error was calculated automatically using the standard pipeline, with the main sources primarily being telluric absorption in the Earth's atmosphere and interpolation over stellar lines in the standard spectrum, with smaller contributions from the calculation of spectral response and readout noise. Smoothing the spectral image cubes to SpeX resolution was seen to reduce random error to negligible values by comparison. However, it also introduced additional sources of systematic uncertainty due to spectral correlation, as well as systematic 'bias' errors from oversmoothing over regions with a high density of solar spectral and telluric lines, a consequence of the 'bias-variance dilemma' (Geman et al., 1992). This bias was quantified simply by taking the difference in radiance at a given wavelength (at SpeX resolution) before and after the smoothing process. An additional systematic error term was also added onto the total spectral error term, in order to encompass various sources of uncertainty in the forward model that are generally difficult to quantify. These include a) a combination of experimental uncertainties in the measurement of the reference gas absorption data, b) uncertainties that result from the use of the correlated-k approximation instead of the line-by-line method, and c) uncertainties that result from other approximations made in the radiative-transfer equation. We found that adding an additional 1% spectral error of the measured flux at each wavelength was sufficient to obtain values of the normalised goodness of fit, $\chi^2/n$, at or below 1 in the majority of Jovian spectra. The

126 contribution of all these factors to the total spectral uncertainty is shown in Figure
127 2.

128 We used two main tests to verify the photometric calibration of each dataset.
129 The first was to disc-average each of the three datasets and cross-calibrate them
130 with the two disc-averaged spectra of Karkoschka (1994) and Karkoschka (1998),
131 respectively calculated from observations of Jupiter in 1993 and 1995, with the
132 latter considered to be of superior quality than the former due to better observ-
133 ing conditions. In the case of the MUSE datasets, the radiance values were
134 converted to I/F using the extraterrestrial solar spectrum of Chance and Kurucz
135 (2010). However, Jupiter's appearance changes over both time and longitude, and
136 so another external source of data, obtained closer in time to the MUSE observa-
137 tions, is required to fully verify the calibration. For this reason, we make use of
138 data from the HST/WFC3 instrument, obtained as part of the OPAL programme
139 (Simon et al., 2015). This data includes two sets of fully-calibrated and projected
140 global observations of Jupiter per year, between 2015 and 2018, as viewed in five
141 wavelength filters that overlap with the MUSE wavelength range (F502N, F547M,
142 F631N, F658N and FQ889N, each named according to the central wavelength
143 in nanometres). Reliable cross-calibration between the MUSE and HST/WFC3
144 datasets is, however, still complicated by both longitudinal variation and the fact
145 that an empirical Minnaert correction has been applied to the HST/WFC3 datasets
146 which increases the disc-averaged I/F. When we multiply the MUSE datasets by
147 each of the five filter functions and then perform our own empirical Minnaert
148 correction on them, we find that even very small uncertainties in the Minnaert
149 coefficients can lead to edge effects at viewing zenith angles close to $90^o$ that
150 can wildly distort the resulting disc-average. To minimise the effect of the uncer-
151 tainty of the Minnaert correction on the cross-calibration, we simply average each
152 MUSE dataset, following filtering and Minnaert correction, within $60^o$ of latitude

either side of the equator and within $10^o$ either side of the sub-observer longitude (a 'swath-average'), and then do the same with the HST/WFC3 datasets obtained closest in time and averaged around the same sub-observer longitude.

As we show in Figure 3, the general shape of each of the three disc-averaged MUSE spectra correspond well with those of Karkoschka (1994) and Karkoschka (1998), and we observe a particularly low systematic offset in I/F between the Karkoschka (1998) disc-averaged spectrum and the 2017-05-15T02:01:59.328 and 2018-04-09T06:04:06.918 disc-averaged spectra respectively. We also observe the swath-averages of the two MUSE datasets to be within 5% of those observed by the OPAL programme on the 3rd of April 2017 and the 17th of April 2018 respectively, with the only major discrepancy being at the F658N filter in the 2018 datasets, which is a part of the spectrum that is dominated by a solar spectral line and for which there is therefore some uncertainty in the calculation of I/F. However, we observe a far greater systematic offset between the 2014-02-17T02:07:56.907 disc-averaged MUSE spectra and both the Karkoschka spectra and the HST/WFC3 latitudinal average. This discrepancy is only partly explicable by the considerable time that elapsed between the obtention of the 2014-02-17T02:07:56.907 MUSE dataset and the obtention of the first set of OPAL data on the 19th of January 2015, since Mendikoa et al. (2017) only find a major decrease in I/F in the North Tropical Zone during this time, which is not enough to fully explain the offset in the latitudinal average. In addition, this offset in the MUSE data results in I/F values in the EZ consistently much greater than 1, which is unphysical and results in atmospheric retrievals that do not converge to a proper solution. We find that we require a systematic decrease in I/F of 20% over all wavelengths in order to have I/F values consistently less than 1 over the whole of Jupiter in this particular dataset. This generally results in the MUSE spectra being correct to within 5% of both the Karkoschka and HST/WFC3 data, with some dis-

crepancy in the F502N filter possibly due to changes in the GRS. Nonetheless, the relatively poor calibration of the 2014 data needs to be taken into account when interpreting our atmospheric retrievals, particularly of tropospheric cloud opacity which is most affected by systematic offsets in I/F.

## 3. Model description

### *3.1. Reference atmosphere*

We made use of the NEMESIS radiative-transfer and retrieval algorithm (Irwin et al., 2008) in order to model all our MUSE spectra. This works by splitting a reference Jovian atmosphere into a number of discrete homogeneous layers (we use 39 in this analysis), and solving the radiative-transfer equation in each layer, taking into account multiple scattering of aerosols, according to the doubling-adding method (Plass et al., 1973), with the state vector iteratively adjusted according to a Levenberg-Marquardt scheme (Rodgers, 2000) in order to provide the best fit to the observed spectra through the optimal estimation method.

The reference atmosphere covered pressure values from a deep limit of 10 bars (90km below the 1 bar reference level) to a high-altitude limit of 1 mbar (150km above the 1 bar level); both altitudes lie far outside MUSE's sensitivity range. The 39 homogeneous layers of the reference atmosphere were spaced closer together in the regions of greatest vertical sensitivity (peaking at intervals of approximately a tenth of a pressure scale height between 0.1 and 2 bars) but further apart in regions of lesser vertical sensitivity. The temperature-pressure profile from the high stratosphere down to 0.8 bars was obtained by averaging a range of temperature profiles inverted from Cassini/CIRS observations of Jupiter acquired during the 2000 flyby (Fletcher et al., 2009), which was then extrapolated to deeper altitudes using a dry adiabat. We neglected spatial variations in temperature, for which no information could be retrieved from visible and near-infrared spectra. Deep

volume mixing ratios of $H_2$, He and $CH_4$ were set to 0.86, 0.134 and $1.8 \times 10^{-3}$ respectively (Niemann et al., 1998; von Zahn et al., 1998), while our prior gaseous ammonia profile was based on that of Fletcher et al. (2009).

### *3.2. Gas absorption models*

By far the greatest sources of gas absorption in this wavelength regime are methane and ammonia. Accurate methane line lists are lacking at these wavelengths, and so methane absorption data was modelled according to Karkoschka and Tomasko (2010) from a combination of measurements in the laboratory and methane transmission measurements through Titan's atmosphere obtained from the Huygens probe. Each absorption band was approximated with a Goody-Voigt band model (Goody and Yung, 1995), and then k-tables computed through exponential line fitting (Irwin et al., 2018). Ammonia absorption data were obtained from the new Coles et al. (2018) line list, with k-distributions computed as in Irwin et al. (2019a). The presence of hydrogen gas in Jupiter also induces substantial absorption around 810-830 nm, primarily due to collision-induced absorption (CIA) of $H_2$ - He and $H_2$ - $H_2$, which we modelled according to Borysow and Frommhold (1989) and Borysow et al. (2000) respectively, as well as some additional, very narrow quadrupole absorption lines for which we used the line lists found in the HITRAN database (Rothman et al., 2013). We neglected the modelling of higher-order CIA and quadrupole absorption lines between 620 nm and 640 nm, which are not discernable in our MUSE spectra and for which accurate line data are not present in the literature. We make use of the correlated-k approximation (Goody et al., 1989) when modelling methane-, ammonia- and quadrupole $H_2$ gas absorption, whose k-distributions are then combined according to the overlapping line approximation (Lacis and Oinas, 1991) in order to save computational time. Rayleigh scattering cross-section computation codes were obtained from Sromovsky (personal communication) and modelled using standard theory (eg.

Goody and Yung, 1995), as explained in detail in Irwin et al. (2019b). The reference extraterrestrial solar spectrum, used to convert radiance values into I/F, was obtained from Chance and Kurucz (2010). All our k-tables and our solar spectrum were smoothed using a triangular instrument function with a FWHM of 2 nm in order to be compatible with the MUSE spectra (or using a Gaussian instrument function with a FWHM of 7 nm when performing retrievals on VIMS spectra).

### 3.3. Cloud and chromophore model

In this analysis we wished to characterise three main populations of aerosols according to the information contained within the MUSE spectra: a thick tropospheric cloud layer of large conservatively-scattering particles, a high-altitude haze layer of small conservatively scattering particles, and a layer of chromophore particles which we assumed were responsible for all the blue-absorption seen on Jupiter. Throughout the rest of this paper we will therefore refer to these particle populations as 'cloud', 'haze' and 'chromophore' respectively. We modelled both the cloud and haze layers as continuous abundance profiles in order to make the best use of the vertical resolution provided by the MUSE spectra, the haze profile occupying the upper half of the atmosphere and the cloud profile occupying the lower half, separated by a narrow boundary layer at 0.15 bars (a pressure level which we found provided the best fit to spectral limb-darkening in both the EZ and NEB at 890 nm, although in practice we are only weakly sensitive to pressure levels below this when observing at single geometries) as shown in Figure 4. Both profiles were sampled at intervals of half a pressure scale height where vertical sensitivity was greatest (between 0.1 and 2 bars) and with more minimal sampling where vertical sensitivity was poorer.

By contrast, we modelled the chromophore layer using a Gaussian profile, with optical depth as a function of pressure $\tau_c(P)$ parametrised according to the following equation:

$$\tau_c(P) = \tau_{c0} \exp\left(-\left(\frac{\ln(P/P_c)}{\Delta_c}\right)^2\right)$$

where $\tau_{c0}$ is the peak optical depth value and $P_c$ the pressure level at which this occurs, which are both allowed to vary freely. Little information can be derived on the chromophore vertical extent $\Delta_c$ from the MUSE spectra, and so we chose to use a value $\Delta_c = 0.25$. This was seen to be narrow enough to facilitate reliable comparison with the so-called *Crème Brûlée* model of Baines et al. (2019), which modelled a chromophore layer with very narrow vertical extent, but wide enough for $P_c$ to be reliably retrieved given the vertical resolution of the reference atmosphere. The choice of FWHM has no measurable influence on the chromophore imaginary refractive index, and only a weak influence on the retrieved chromophore pressure level. We chose this approach over the so-called *Crème Brûlée* model of Baines et al. (2019) for several reasons: firstly, it prevented the retrieval of chromophore altitude from interfering with retrievals of cloud and haze, and secondly, it allowed for the modelling of an upper-tropospheric haze layer around 0.2-0.3 bars to fit the strong 890 nm methane absorption feature that could be decoupled from tropospheric cloud located at higher pressures. At this wavelength range, there is very little sensitivity to stratospheric haze ($p < 0.15$ bars) from single-geometry observations, except at the poles which are observed at high viewing zenith angle and where the haze is particularly opaque. To constrain stratospheric haze opacity close to nadir, we require information at wavelengths below approximately 420 nm (Fry and Sromovsky, 2018). For a more detailed breakdown of the more stylistic differences between the *Crème Brûlée* model and our own, we refer the reader to the thesis of Braude (2019). For reference, we will also compare some of the retrievals that we have conducted using this model with those using the *Crème Brûlée* model where stated, using a modelling approach as close to that of Sromovsky et al. (2017) as we can replicate.

Although cloud and haze particles in Jupiter's atmosphere are solid and therefore non-spherical, we assume that a large ensemble of non-spherical particles can be modelled as spherical Mie scatterers using the code of Dave (1968). We then approximate the resulting Mie phase functions using a double Henyey-Greenstein phase function (Henyey and Greenstein, 1941), as calculated using a Levenberg-Marquardt scheme that minimises the least-squares deviation from the Mie phase function, in order to smooth over features of the Mie phase functions that are unique to spherical particles. A comparison of these two phase functions is shown in Figure 5.

## 4. Retrieving a universal chromophore

### *4.1. Limb-darkening analysis*

To test the hypothesis of a universal chromophore, we first extracted a representative latitudinal swath of the NEB between $10^o$N and $13^o$N (planetographic) from our primary MUSE observation in April 2018, which is shown graphically in Figure 6. At this point in time, the southern NEB was the reddest region of Jupiter after the GRS, was relatively homogeneous in appearance with longitude in comparison with the South Equatorial Belt (SEB) and had little high-altitude haze cover, making the fitting of chromophore more straightforward to decouple from other atmospheric variables than in other regions of Jupiter. The shape of the limb-darkening curve along the swath was seen to be well modelled if the swath was sampled at each wavelength at longitude values of $\{-60^o, -30^o, 0^o, 30^o, 60^o\}$ relative to the central meridian, avoiding large viewing zenith angles close to the outer perimeter of Jupiter's planetary disc where mixing with the sky is significant. Each longitude sample was obtained by computing a Gaussian weighted average of all spectra within a FWHM of 3 degrees of longitude. The respective spectral errors were then found through the standard deviation of the Gaussian

weighted average. In order to save computational time, only 200 wavelengths per spectrum (giving 1000 wavelengths in total) were fit in our limb-darkening analysis, selected according to both information content (Rodgers, 1996; Ventress and Dudhia, 2014) and to model the shapes of the main absorption features optimally. These wavelengths were therefore mainly concentrated in regions of high methane and ammonia absorption, as well as below 600 nm, while avoiding regions of low signal-to-noise (such as around 760 nm).

In Figure 7 we show clearly that the chromophore of Carlson et al. (2016) provides an inadequate fit to the spectral slope of the NEB below 600 nm, even when accounting for variations in particle size distribution, using the *Crème Brûlée* model alone. We therefore chose to retrieve the imaginary part of the refractive index spectrum of the chromophore, $k_c(\lambda)$, directly from spectral limb-darkening of the NEB, sampled at 50 nm intervals between 450 nm and 950 nm using the optical constants of Carlson et al. (2016) as a prior. We found that particle-size distributions could only be weakly constrained from limb-darkening, especially that of chromophore, but had a major effect on the retrieved chromophore absorption spectrum. Our approach was to therefore model all three particle populations using a gamma size distribution with a fixed variance of 0.05, and with the effective radius of the cloud ($r_n$) and chromophore ($r_c$) particles fixed to different values for individual retrievals chosen to maximise the parameter space searched, and the haze effective radius ($r_h$) allowed to weakly vary from a prior value of 0.5 μm. These were all selected in line with values in the literature (notably Stoll (1980); Ragent et al. (1998); West et al. (2004) and McLean et al. (2017)). We fixed the real parts of the refractive index spectra of both the chromophore ($n_c$) and haze ($n_h$) particles to 1.4 at a wavelength of 700 nm, but fixed that of the cloud particles to several different values from 1.42 (equivalent to ammonia ice according to Martonchik et al. (1984)) to 1.6. A detailed key of the fixed and variable

parameters of our model is shown in Table 2.

We were unable to fit the swath with a goodness of fit value ($\chi^2/n$, where n = 1000) less than 1 for any prior parameter, and within the parameter space searched in this analysis, only solutions where $r_n = 1.0\mu m$ and $n_n = 1.42$ could provide a fit with $\chi^2/n < 1.2$. Of these, two sets of solutions were found to be applicable to within uncertainty of the lowest $\chi^2/n$ value (where the uncertainty is given by $\sigma_{\chi^2/n} = \sqrt{2/n} = 0.45$): one where $r_c < 0.1\mu m$ and one where $r_c > 0.5\mu m$, as shown in Figure 8. Raising $n_n$ a small amount could also provide reasonable $\chi^2/n$ values so long as $r_n$ was lowered to compensate, but if $n_n$ was set to 1.6 or above we obtained very poor fits at high viewing zenith angles to the methane absorption feature at 619 nm regardless of particle size distribution. This was contrary to the findings of Sato et al. (2013) who obtained a value of $n_n$ closer to 1.85 in the South Tropical Zone (STropZ) from Cassini/ISS measurements. We should note that Howett et al. (2007) state a real refractive index for $NH_4SH$ of 1.75 at visible and near-infrared wavelengths, but they only provide citations of this value through personal communication. Nonetheless, if this value can be independently verified, then it would indicate that the deepest cloud layer we observe in the visible and near-infrared is not made primarily of $NH_4SH$, at least in the NEB.

Although the retrieved chromophore imaginary refractive index spectrum changes substantially with $r_c$, our solutions all have several features in common. In all cases, we require a spectral slope between 476 nm and 600-650 nm that is greater than can be provided by the chromophore of Carlson et al. (2016), as shown in Figure 9 and Table 3. Usually, our model does this by raising the imaginary refractive index at the shortest wavelengths, and decreasing it at longer wavelengths relative to Carlson et al. (2016). We also retrieved a secondary absorption peak around 850 nm, although this could be a result of uncertainties in methane band absorption data as opposed to a genuine chromophore absorption feature. How-

ever, we should clarify that the experimental uncertainties on the optical constants of the chromophore of Carlson et al. (2016) were not published, and so it is possible that the uncertainty in the thickness of the chromophore film produced in the laboratory, or some other factor, may affect the value of the imaginary refractive index spectrum they derive. We therefore cannot rule out the possibility of red colour on Jupiter forming in a manner similar to that of the chromophore of Carlson et al. (2016).

We should note that, using the model described in section 3.3, but still fixing $k_c(\lambda)$ to the optical constants of Carlson et al. (2016), we were still able to provide a much better fit to the spectra than using the *Crème Brûlée* model, with the best results obtained when $r_n = 1\mu m$, $r_c = 0.1\mu m$ and $n_n = 1.42$, and with a fit to the spectrum not far removed from the case where we retrieved $k_c(\lambda)$ directly, with $\chi^2/n = 1.48$. Nonetheless, we chose to stick with our own retrieved chromophore absorption spectrum for a number of reasons. Firstly, our retrieved chromophore absorption spectrum did provide some improvement to the fit to the shape of the blue-absorption gradient, particularly at lower viewing zenith angles. We also remark on the fact that the increase in the retrieved blue-absorption gradient relative to the chromophore of Carlson et al. (2016) is consistent regardless of the values of $r_n$, $r_c$ or $n_n$ we choose. However, we find that the greatest justification for retrieving the chromophore absorption spectrum directly is through fitting of the GRS, as we describe in the next section.

### *4.2. Selection of a universal chromophore*

In order to confirm whether any chromophore solution retrieved from the NEB could be deemed that of a 'universal chromophore', we must by definition be able to apply the same chromophore solution to any spectrum of Jupiter and obtain a fit to the spectral slope below 600 nm that is adequate. In addition, the resulting retrieved aerosol abundances should be in line with theoretical expectations as well

as with other prior observations of Jupiter. We first attempted to fit each 'well'-retrieved chromophore imaginary refractive index solution, defined as those for which $\chi^2/n < 1.3$ in the NEB and for which $r_h < r_n$ (in order to be physical), to a single spectrum extracted from the centre of the GRS as observed in April 2018. This spectrum was selected as it had the greatest spectral slope at blue wavelengths found anywhere on Jupiter, and was the most difficult spectrum to model using the chromophore of Carlson et al. (2016). Unlike with the aforementioned limb-darkening analysis, we fit all 435 wavelengths between 476 nm and 910 nm of the spectrum of the GRS; wavelengths above 910 nm were seen to be overly affected by second-order contamination and were therefore cropped out. As in the previous section, a detailed list of fixed and variable parameters is shown in Table 2. In order to better compare our retrieved aerosol density values with those in the literature, usually quoted in units of g/l, we have assumed cloud, haze and chromophore particle mass densities to all be equal to 0.87g/cm$^3$, equivalent to that of ammonia ice (Satorre et al., 2013). A corresponding mass density value for $NH_4SH$ is lacking in the literature, but we assume that it is approximately triple that of $NH_3$ ice based on the difference in molecular weight.

As shown in Table 4, we found that it was often simpler to fit chromophore solutions with higher values of $n_n$ to the GRS than it was with lower values. However, we find that the retrieved cloud densities also drop dramatically with increasing $n_n$: as one increases the value of $n_n$ from 1.4 to 1.6, the retrieved cloud densities drop by approximately a factor of 10 for given values of $r_n$ and $r_c$, and in practice, given the lower best-fit values of $r_n$ for solutions with increasing $n_n$, the decrease in retrieved cloud density is even more substantial. Palotai et al. (2014) estimated consistent aerosol mass densities in the centre of the GRS of the order of $10^{-5}$ g/l over all visible altitudes using a general circulation model, while Zuchowski et al. (2009) estimated average $NH_4SH$ cloud mass densities in

the STropZ, one of the cloudiest bands on Jupiter, of the order of $10^{-6}$ g/l. By contrast, the Galileo Probe Nephelometer retrieved maximum mass densities of the order of $10^{-7}$ – $10^{-6}$ g/l (Ragent et al., 1998) at its entry site in a hotspot region where aerosol densities are predicted to be exceptionally low by Jovian standards, and certainly lower than the GRS. This makes it very difficult to justify the retrieved values of cloud density of the order of $10^{-8}$-$10^{-7}$g/l in the GRS if $n_n$ is increased well above that predicted for ammonia ice, or even to 1.5 which is within the margin of error of laboratory measurements of the refractive index of ammonia ice (quoted as 1.48 in both Romanescu et al. (2010) and Satorre et al. (2013)). Prior constraints from the literature, together with our own from limb-darkening in the NEB, would therefore rule out a high $n_n$ solution even if they provided a good fit to the GRS (we did not test solutions for $n_n$ lower than 1.42 due to the absence of substances likely to be present in Jovian clouds with such a low refractive index, other than water ice which freezes out of the atmosphere at pressure levels not observable in the MUSE spectral range). We also note that the higher the value of $r_c$, the greater the retrieved mass density of the cloud layer. However, we obtained an inferior fit to the spectrum of the GRS if we raised $r_c$ to 0.5 μm. As a compromise, we therefore chose our 'universal chromophore' solution as the one where $r_n = 1\mu m$, $r_c = 0.05\mu m$ and $n_n = 1.42$. This resulted in a cloud mass density of approximately $(1.7 \pm 0.1) \times 10^{-6}$ g/l - on the lower end of predicted mass densities for Jovian clouds, but not entirely unrealistic.

The fit of this optimal chromophore solution to spectra of the GRS before and after the reddening events reported by Simon et al. (2014, 2018) are shown in Figure 10. We found the fits to be adequate in both cases, unlike those provided by the optical constants of Carlson et al. (2016) particularly following the most recent reddening event. The only way in which we are able to fit the GRS spectrum in 2018 using the optical constants of Carlson et al. (2016) is to raise $r_n$ to 1.6, but

this would result in the underestimation of cloud opacity for reasons previously discussed. This therefore begs the question as to why our results contradict those of Sromovsky et al. (2017) so substantially, who were able to provide a good fit to their own Cassini/VIMS spectra of the GRS using the chromophore of Carlson et al. (2016). The most likely reason is that, while the most dramatic reddening has only occurred in the past few years, the blue-absorption gradient of the spectrum of the GRS had been gradually but consistently steepening at least since the Voyager era. This means that VIMS spectra of the GRS obtained during the Cassini flyby in 2000, as well as MUSE spectra obtained in 2014, were substantially easier to fit using the Carlson et al. (2016) optical constants than MUSE spectra from 2018, as we also show clearly in figure 10. Nonetheless, we should also note that the general fit to the Cassini/VIMS spectrum of the GRS from 2000, as calibrated and supplied by Carlson et al. (2016), is poorer than to the MUSE spectra from 2014 and 2018, regardless of the model used. We believe that this can mostly be blamed on deficiencies in the VIMS calibration. The shape of the methane absorption features at 727 nm and 880 nm in particular are both unphysical and difficult to fit, even when taking into account the lower spectral resolution relative to MUSE in the reference gas absorption data, and this is clearly seen when compared to the smoothed disc-averaged spectra of Karkoschka (1994, 1998) by both Sromovsky et al. (2017) and Baines et al. (2019).

In all cases, we retrieved relatively consistent chromophore abundances in the GRS regardless of $r_c$ of the order $10^{-8}$ g/l, which is also in agreement with the findings of Sromovsky et al. (2017), but would require a flux rate of acetylene into the tropopause to produce that is at least a factor of 10 higher than that predicted through photochemistry alone (Moses et al., 2010).

## 5. Application of universal chromophore

### *5.1. Fits to representative spectra*

We now discuss the fit of our universal chromophore solution in relation to spectra from three different locations on Jupiter other than the GRS, as shown in Figure 11, and with retrieved cloud and chromophore vertical profiles given in Figure 12. Each was chosen to represent the three main spectral morphologies one typically finds on Jupiter (excluding polar and hotspot regions): high continuum reflectivity with low blue-absorption (the Equatorial Zone, or EZ for short), low continuum reflectivity with high blue-absorption (the NEB), and high continuum reflectivity with high blue-absorption (the NTBs and GRS). Wavelengths below 600 nm were fit well within the uncertainty boundaries for the belts and the GRS. When it comes to the EZ, however, we can see that the fit to shorter wavelengths is noticeably inferior to other regions of Jupiter, even when variations in particle size are accounted for. We focus on the spectral region that consistently caused the greatest perturbation to the blue-absorption slope, which is between approximately 510 and 540 nm, where we discern a small increase in I/F in the EZ and the NTBs relative to the NEB and the GRS, which was not accounted for in our retrieved chromophore absorption spectrum. Unfortunately, this is a wavelength region with a somewhat low signal-to-noise ratio (averaging around 20-30 between 510 and 540 nm, as opposed to ~60-100 at continuum near-infrared wavelengths) due to the uncertainty in the interpolation of stellar lines when calibrating the spectra. Nonetheless, we assume this variation is genuine as it does not appear to be either random or systematic over the surface of Jupiter. The variability in I/F at these wavelengths could be due to a number of factors: a) a genuine secondary chromophore absorption feature (perhaps due to an $n \rightarrow \pi^*$ transition (Nassau, 1983)) that could be characteristic of a certain molecular endmember, b) a consequence of other properties of the atmosphere that we have not properly accounted

for, but which might alter the local blue-absorption gradient (such as the presence of additional aerosol or gas layers, or local changes in temperature and pressure that could alter the molecular structure of the chromophore and hence the breadth of its primary absorption feature), or c) poor band data around the 540 nm methane absorption feature. This particular feature aside, however, our spectral fits show that we cannot entirely rule out the possibility of a universal chromophore. To either confirm or reject this universal chromophore solution definitively, we would require spectral information at wavelengths shorter than the lower limit of 475 nm provided by MUSE's nominal wavelength range.

For comparison, we have also included absorption spectra of irradiated $NH_4SH$, itself a candidate chromophore as proposed by Lebofsky and Fegley (1976) and more recently by Loeffler et al. (2015, 2016). We can see that the shape of these absorption spectra model blue-absorption poorly on Jupiter for two main reasons. One is that the reflectance spectrum of irradiated $NH_4SH$ only appears to show substantial absorption below 500 nm, whereas the shortwave absorption peak in Jovian spectra extends all the way to 600 nm. This discrepancy may be alleviated by altering the altitude of the irradiated $NH_4SH$ particles or changing their size distribution, but this is difficult to verify due to the absence of $NH_4SH$ optical constant data below 1000 nm in the literature. The other issue pertains to the presence of a secondary broad absorption peak at around 610 nm due to $S_3^-$ radicals, which is completely absent in Jovian spectra. This extra absorption peak is known to disappear under only two circumstances: a) the $NH_4SH$ is irradiated at temperatures far below even the coldest temperatures found on Jupiter (Loeffler and Hudson, 2018), or b) the $NH_4SH$ is irradiated at temperatures typically found in the upper troposphere, but is then reheated to temperatures one would only expect around 2 bars, substantially below the maximum visible penetration depth even in the belts (Loeffler et al., 2016). We will therefore rule out irradiated

525 $NH_4SH$ as a candidate chromophore in this work until a plausible hypothesis can
526 be found to explain these two discrepancies.

527 *5.2. Modelling meridional variations in tropospheric aerosol structure*

528 Having established that our universal chromophore solution could provide a
529 mostly good fit to representative spectra of Jupiter, we then applied this solution
530 more generally to look at overall meridional variations in cloud structure, chro-
531 mophore abundances and cloud-top gaseous ammonia abundances on Jupiter. We
532 extracted a swath of single-pixel width, as shown at different wavelengths in Fig-
533 ure 6, at a longitude chosen to minimise the viewing zenith angle of observation of
534 each latitude, but also to prevent the bisection of longitudinally anomalous regions
535 in order simply to observe 'generic' zone-belt variations (although in practice,
536 given the turbulent nature of the northern NEB at this time, this was not entirely
537 possible). We did not analyse latitudes for which the viewing zenith angle was
538 greater than $60^o$, for several reasons: a) to save computational time (due to the
539 increased number of quadrature points required to perform integration over view-
540 ing zenith and azimuthal angles closer to the limb), b) to avoid spectral mixing
541 with the sky, a consequence of MUSE's relatively low spatial resolution and un-
542 certainties in the PSF, and c) we were unable to model variations in the spectral
543 fit around 890 nm in the polar regions (as can be seen in Figure 13), even if we
544 accounted for a thick stratospheric 'polar hood'. In total, we therefore performed
545 spectral analysis on 173 individual spectra in the swath, obtained at single-pixel
546 resolution. We performed this analysis only on a single Jupiter observation (2018-
547 04-09T06:04:06.918) due to its optimal observing conditions and calibration, even
548 though this observation took place during notable meteorological events for which
549 retrieved atmospheric parameters in certain latitudinal bands (particularly the EZ
550 and NEB) may have been unique to that particular time. A broader analysis of
551 temporal changes in colour and cloud structure between 2014 and 2018 is beyond

552 the scope of this paper, as are variations in cloud-top ammonia gas abundances
553 which are highly model-dependent and variable in time and longitude. We refer
554 the reader instead to the thesis of Braude (2019) for more information on these
555 changes.

556 The results of our analysis are shown in Figure 13. As the belts are thought to
557 be regions of net downwelling, we would expect the altitude of the cloud layer to
558 be deeper here than in the zones. In addition, a lack of cloud and haze cover in the
559 belts would allow for the observation of deeper layers than in the zones. However,
560 we observe a relative lack of variation in the altitude of the main cloud layer, usu-
561 ally retrieved around (1.4±0.3) bars in both the zones and the belts (although the
562 altitude of the cloud in the belts is more poorly-defined, as can be seen in Figure
563 12), in line with the observations of Irwin et al. (1998, 2001) and Sromovsky and
564 Fry (2002). This invariance cannot be a consequence of a constant temperature-
565 pressure profile between the zones and the belts, as we found that varying the
566 temperature profile systematically by 5 K, in line with measured zone-belt vari-
567 ations in temperature in the upper troposphere (Fletcher et al., 2016), produced
568 no effect on the retrieved cloud altitude. We also found no evidence of a dis-
569 crete cloud layer near the ammonia condensation level as found by Banfield et al.
570 (1998) and Simon-Miller et al. (2001) in the visible and near-IR, or as required in
571 the mid-IR (eg. Matcheva et al., 2005). This cannot simply be explained by effects
572 of the model, as suppressing prior cloud densities below the predicted ammonia
573 cloud level, usually estimated around 0.7 bars (eg. Atreya et al. (1999)), leads to a
574 very poor fit to continuum wavelengths regardless of particle size distribution, as
575 we show clearly in Figure 14. Even in the EZ, in which net upwelling is thought
576 to be at its strongest, we always required a thick cloud layer deeper than the 1-bar
577 level to fit our spectra. It is predicted to be too warm at these altitudes for am-
578 monia ice to condense out of the atmosphere, and so these cloud layers cannot be

579 made of ammonia ice. Although ECCMs usually predict an $NH_4SH$ cloud to be
580 located deeper than our retrieved altitude (around 2.2-2.6 bars as estimated eg. by
581 Atreya et al. (1999)), the cloud could be located at a higher altitude if the $H_2S$ mix-
582 ing ratio is suppressed, or if the cloud is made of a different sulphur compound.
583 However, this would conflict with our observations of NEB cloud which appear to
584 have a low real refractive index. We are unable to reconcile these two conflicting
585 observations without speculation, perhaps invoking the presence of ammonia and
586 water ice 'mushballs' that circulate around the main cloud layers as hypothesised
587 by Guillot et al. (2019). It is also possible that the apparently missing $NH_3$ cloud
588 is in fact present in the zones, but cannot be resolved in our data either from the
589 main 1.4-bar cloud layer or from the upper tropospheric hazes due to a lack of
590 vertical resolution.

591 In spite of the invariance of the main cloud altitude, we generally observed the
592 zone-belt variations in colour, cloud structure and ammonia abundance that we ex-
593 pected to find. The zones were associated with thicker cloud, less colour, greater
594 cloud-top ammonia abundances, larger particle sizes and greater haze thickness
595 than the belts. Upper tropospheric haze was concentrated around the EZ, as it
596 has been since the year 2000 (Lii et al., 2010), and stratospheric haze thickest
597 and highest towards the poles. We found that the STropZ had cloud opacities
598 larger that those of the EZ, an observation that the reflectivity measurements of
599 Mendikoa et al. (2017) would also lend some credence to. After the GRS, the
600 southern NEB was the reddest region of Jupiter; although the NTBs ws still red at
601 this time, its colour was not as prominent as it had been in 2017 as shown in Table
602 5. This shows that our model provides valid results on the properties of Jupiter's
603 atmosphere. However, we did obtain some results that defied our expectations.
604 One was the surprising lack of cloud cover even in the southern part of the EZ that
605 was relatively unaffected by the colouration event that started around that time

(Antuñano et al., 2018), which was comparable in its thickness to that found in the northern NEB due to mixing from the North Tropical Zone (NTropZ). Surprisingly high chromophore abundances are retrieved in the northern half of the EZ, even though the colouration event was still in its infancy at this stage. We also note that the region where the red NTBs colour was still prominent was barely distinct from the surrounding region in terms of either cloud structure or gaseous ammonia abundances, which it was in early 2017 when it was associated with thick cloud and haze cover. This may hint at chromophore in this region that is located in a stable region of the atmosphere unaffected by the weather below it.

Unfortunately, chromophore abundances outside the GRS were insufficient even in the NEB to completely constrain their altitude in the atmosphere, as we lack the wavelengths below 475 nm that are sensitive to the stratosphere. However, they were sufficient in the belts to constrain a 'lower bound' on their likely altitude, that is, the deepest pressure level that the chromophore could be located at. This is usually around (0.6±0.1) bars, well above the retrieved altitude of the deepest visible cloud layer, but located at approximately the level of the predicted ammonia ice cloud layer. We therefore cannot rule out zone-belt differences in colour being due to the sublimation of ammonia ice rime in the warmer belts to reveal chromophore nuclei.

## 6. Conclusions

We analysed three spectral image cubes of Jupiter, obtained between 2014 and 2018 in the visible and near-infrared (480-930 nm) from the VLT/MUSE instrument, in order to a) characterise the absorption spectrum of Jupiter's colour-carrying compounds ('chromophores') and whether it could be applied uniformly to model all blue-absorption on Jupiter (a 'universal chromophore'), and b) to analyse spatial variability in colour and cloud/haze structure over Jupiter's surface.

This was performed using a three-cloud model, consisting of two conservatively-scattering layers corresponding to deep cloud and high-altitude haze respectively, and a single chromophore layer whose absorption spectrum was found by directly retrieving the imaginary part of its refractive index. Our main conclusions were as follows:

- As we were able to fit the shape of the shortwave spectral feature of both the belts and the GRS well using the same chromophore compound, we cannot rule out the possibility of a universal chromophore as proposed by Sromovsky et al. (2017). However, in order to fit the most recent observations of the GRS following its recent intensification in colour, we found that this chromophore compound required steeper blue-absorption than could be provided by the tabulated optical constants of Carlson et al. (2016) in order to be in keeping with previous constraints on the opacity of the main cloud layer. This is nonetheless in keeping with a chromophore production mechanism involving photolysed ammonia reacting with acetylene as proposed by Ferris and Ishikawa (1987, 1988), although the issue with the predicted relative absence of acetylene that would be required to produce chromophore in the troposphere according to this mechanism remains to be resolved.

- We identified some spectral variability between 510 and 540 nm that, while well within the spectral error constraints provided by VLT/MUSE, does alter the shape of the blue-absorption gradient found in spectra throughout Jupiter, which we were unable to model through changes in cloud particle size alone. This could potentially be due to a secondary chromophore absorption feature, for which we recommend further investigation.

- Although the exact vertical location of chromophore was difficult to con-

strain given our wavelength range, we had sufficient information to constrain a 'lower bound' on how deep the chromophore could be located. In the belts, we found that the chromophore could not be located deeper than around $0.6 \pm 0.1$ bars, approximately equivalent to the predicted location of the ammonia ice cloud layer on Jupiter. In the GRS on the other hand, we found that the chromophore must be located in or above the upper tropospheric haze, around 0.2 bars.

- We retrieved a thick cloud layer whose base altitude varied little from $1.4 \pm 0.3$ bars over the surface of Jupiter. Temperatures are too high at these altitudes for ammonia to condense, and hence this cloud layer could not be primarily made of ammonia ice. On the other hand, we found that the retrieved cloud opacities and particle sizes in the belts and the GRS were in keeping with a cloud layer that had a low refractive index close to that of ammonia ice (1.42, Martonchik et al. (1984)), and could not be as high as 1.85 as was found by Sato et al. (2013). This appears to contradict a cloud layer being made primarily of $NH_4SH$ at these altitudes, whose refractive index is predicted to be substantially larger than that of ammonia ice, and may be the result of overlying ammonia ice masking the signature of the $NH_4SH$ cloud layer.

Facility: VLT/MUSE

## Acknowledgements

This paper makes use of data from the European Southern Observatory (ESO), programme IDs 60.A-9100, 099.C-0192 and 101.C-0097, as well as data acquired from the NASA/ESA HST Space Telescope, associated with OPAL program (PI: Simon, GO13937), and archived by the Space Telescope Science Insti-

683 tute, which is operated by the Association of Universities for Research in Astron-
684 omy, Inc., under NASA contract NAS 5-26555. All maps of the latter are avail-
685 able at http://dx.doi.org/10.17909/T9G593. We thank Larry Sromovsky for his
686 codes to calculate Rayleigh-scattering opacities and Mark Loeffler for providing
687 absorption spectra of irradiated $NH_4SH$. Ashwin Braude was supported through a
688 studentship from the United Kingdom Science and Technology Facilities Council
689 (STFC). Glenn Orton was supported by funding from NASA distributed to the
690 Jet Propulsion Laboratory, California Institute of Technology. Leigh Fletcher was
691 supported by a Royal Society Research Fellowship at the University of Leicester.

## 692 References

693 A. Antuñano, L. N. Fletcher, G. S. Orton, H. Melin, J. H. Rogers, J. Harrington,
694 P. T. Donnelly, N. Rowe-Gurney, and J. S. D. Blake. Infrared Characterisation
695 of Jupiter's Equatorial Disturbance Cycle. *Geophysical Research Letters*, 45:
696 10, 2018. doi: 10.1029/2018GL080382.

697 S. K. Atreya, M. H. Wong, T. C. Owen, P. R. Mahaffy, H. B. Niemann, I. De Pater,
698 P. Drossart, and T. Encrenaz. A Comparison of the Atmospheres of Jupiter and
699 Saturn: Deep Atmospheric Composition, Cloud Structure, Vertical Mixing, and
700 Origin. *Planetary and Space Science*, 47:1243–1262, 1999.

701 R. Bacon, M. Accardo, L. Adjali, H. Anwand, S. Bauer, I. Biswas, J. Blaizot,
702 D. Boudon, S. Brau-Nogue, J. Brinchmann, et al. The MUSE Second-
703 Generation VLT Instrument. In *Ground-based and Airborne Instrumentation
704 for Astronomy III*, volume 7735 of *Proc. SPIE*, page 773508, 2010. doi:
705 10.1117/12.856027.

706 K. H. Baines, L. A. Sromovsky, R. W. Carlson, T. W. Momary, and P. M. Fry.
707 The Visual Spectrum of Jupiter's Great Red Spot Accurately Modeled with

Aerosols Produced by Photolyzed Ammonia Reacting with Acetylene. *Icarus*, 330:217–229, 2019. doi: 10.1016/j.icarus.2019.04.008.

D. Banfield, P. J. Gierasch, M. Bell, E. Ustinov, A. P. Ingersoll, A. R. Vasavada, Robert A. West, and M. J. S. Belton. Jupiter's Cloud Structure from Galileo Imaging Data. *Icarus*, 135:230–250, 1998. doi: 10.1006/icar.1998.5985.

A. Borysow and L. Frommhold. Collision-Induced Infrared Spectra of $H_2$ - He Pairs at Temperatures from 18 to 7000 K. II - Overtone and Hot Bands. *Astrophysical Journal*, 341:549–555, 1989. doi: 10.1086/167515.

A. Borysow, J. Borysow, and Y. Fu. Semi-Empirical Model of Collision-Induced Absorption Spectra of $H_2$ - $H_2$ Complexes in the Second Overtone Band of Hydrogen at Temperatures from 50 to 500 K. *Icarus*, 145:601–608, 2000. doi: 10.1006/icar.2000.6384.

A. S. Braude. *Colour and Cloud Structure in the Atmospheres of the Giant Planets*. DPhil Thesis, University of Oxford, 2019.

R. H. Brown, K. H. Baines, G. Bellucci, J.-P. Bibring, B. J. Buratti, F. Capaccioni, P. Cerroni, R. N. Clark, A. Coradini, D. P. Cruikshank, et al. The Cassini Visual and Infrared Mapping Spectrometer (VIMS) Investigation. *Space Science Reviews*, 115:111–168, 2004. doi: 10.1007/s11214-004-1453-x.

R. W. Carlson, K. H. Baines, M. S. Anderson, G. Filacchione, and A. A. Simon. Chromophores from Photolyzed Ammonia Reacting with Acetylene: Application to Jupiter's Great Red Spot. *Icarus*, 274:106–115, 2016. doi: 10.1016/j.icarus.2016.03.008.

K. Chance and R. L. Kurucz. An Improved High-Resolution Solar Reference Spectrum for Earth's Atmosphere Measurements [sic] in the Ultraviolet, Vis-

ible, and Near Infrared. *Journal of Quantitative Spectroscopy and Radiative Transfer*, 111(9):1289–1295, 2010. doi: 10.1016/j.jqsrt.2010.01.036.

P. A. Coles, R. I. Ovsyannikov, O. L. Polyansky, S. N. Yurchenko, and J. Tennyson. Improved Potential Energy Surface and Spectral Assignments for Ammonia in the Near-Infrared Region. *Journal of Quantitative Spectroscopy and Radiative Transfer*, 219:199–212, 2018. doi: 10.1016/j.jqsrt.2018.07.022.

A. Coradini, G. Filacchione, F. Capaccioni, P. Cerroni, A. Adriani, R. H. Brown, Y. Langevin, and B. Gondet. CASSINI/VIMS-V at Jupiter: Radiometric Calibration Test and Data Results. *Planetary and Space Science*, 52(7):661–670, 2004. doi: 10.1016/j.pss.2003.11.005.

J. V. Dave. *Subroutines for Computing the Parameters of the Electromagnetic Radiation Scattered by a Sphere*. IBM Palo Alto Scientific Center, 1968.

J. P. Ferris and Y. Ishikawa. HCN and Chromophore Formation on Jupiter. *Nature*, 326:777, 1987. doi: 10.1038/326777a0.

J. P. Ferris and Y. Ishikawa. Formation of Hydrogen Cyanide and Acetylene Oligomers by Photolysis of Ammonia in the Presence of Acetylene: Applications to the Atmospheric Chemistry of Jupiter. *Journal of the American Chemical Society*, 110(13):4306–4312, 1988. doi: 10.1021/ja00221a033.

L. N. Fletcher. Cycles of Activity in the Jovian Atmosphere. *Geophysical Research Letters*, 44:4725–4729, 2017. doi: 10.1002/2017GL073806.

L. N. Fletcher, G. S. Orton, N. A. Teanby, and P. G. J. Irwin. Phosphine on Jupiter and Saturn from Cassini/CIRS. *Icarus*, 202:543–564, 2009. doi: 10.1016/j.icarus.2009.03.023.

L. N. Fletcher, T. K. Greathouse, G. S. Orton, J. A. Sinclair, R. S. Giles, P. G. J. Irwin, and T. Encrenaz. Mid-Infrared Mapping of Jupiter's Temperatures, Aerosol Opacity and Chemical Distributions with IRTF/TEXES. *Icarus*, 278: 128–161, 2016. doi: 10.1016/j.icarus.2016.06.008.

P. M. Fry and L. Sromovsky. Using HST Bandpass Filter Images from the OPAL Program to Test the Ability of Candidate Chromophores to Model Spatial and Temporal Variations on Jupiter. In *AAS/Division for Planetary Sciences Meeting Abstracts*, volume 50, page 119.13, 2018.

S. Geman, E. Bienenstock, and R. Doursat. Neural Networks and the Bias/Variance Dilemma. *Neural Computation*, 4(1):1–58, 1992. doi: 10.1162/neco.1992.4.1.1.

R. S. Giles, L. N. Fletcher, and P. G. J. Irwin. Cloud Structure and Composition of Jupiter's Troposphere from 5-$\mu$m Cassini VIMS Spectroscopy. *Icarus*, 257: 457–470, 2015. doi: 10.1016/j.icarus.2015.05.030.

R. Goody, R. West, L. Chen, and D. Crisp. The Correlated-K Method for Radiation Calculations in Nonhomogeneous Atmospheres. *Journal of Quantitative Spectroscopy and Radiative Transfer*, 42(6):539–550, 1989. doi: 10.1016/0022-4073(89)90044-7.

R. M. Goody and Y. L. Yung. *Atmospheric Radiation: Theoretical Basis*. Oxford University Press, 1995.

T. Guillot, D. J. Stevenson, C. Li, S. Atreya, A. Ingersoll, and S. Bolton. Storms and the Distribution of Ammonia in Jupiter's Atmosphere. *European Planetary Science Congress*, 13:EPSC–DPS2019–1142, 2019.

C. J. Hansen, M. A. Caplinger, A. Ingersoll, M. A. Ravine, E. Jensen, S. Bolton,

779 and G. Orton. JunoCam: Juno's Outreach Camera. *Space Science Reviews*,
780 pages 1–32, 2014. doi: 10.1007/s11214-014-0079-x.

781 L. G. Henyey and J. L. Greenstein. Diffuse Radiation in the Galaxy. *The Astro-*
782 *physical Journal*, 93:70–83, 1941. doi: 10.1086/144246.

783 C. J. A. Howett, R. W. Carlson, P. G. J. Irwin, and S. B. Calcutt. Optical Constants
784 of Ammonium Hydrosulfide Ice and Ammonia Ice. *Journal of the Optical*
785 *Society of America B*, 24(1):126–136, 2007. doi: 10.1364/JOSAB.24.000126.

786 P. G. J. Irwin, A. L. Weir, S. E. Smith, F. W. Taylor, A. L. Lambert, S. B. Calcutt,
787 P. J. Cameron-Smith, R. W. Carlson, K. Baines, G. S. Orton, et al. Cloud Struc-
788 ture and Atmospheric Composition of Jupiter Retrieved from Galileo Near-
789 Infrared Mapping Spectrometer Real-Time Spectra. *Journal of Geophysical*
790 *Research: Planets*, 103:23001–23021, 1998. doi: 10.1029/98JE00948.

791 P. G. J. Irwin, A. L. Weir, F. W. Taylor, S. B. Calcutt, and R. W. Carlson. The Ori-
792 gin of Belt/Zone Contrasts in the Atmosphere of Jupiter and their Correlation
793 with 5-$\mu$m Opacity. *Icarus*, 149:397–415, 2001. doi: 10.1006/icar.2000.6542.

794 P. G. J. Irwin, N. A. Teanby, R. De Kok, L. N. Fletcher, C. J. A. Howett, C. C. C.
795 Tsang, C. F. Wilson, S. B. Calcutt, C. A. Nixon, and P. D. Parrish. The NEME-
796 SIS Planetary Atmosphere Radiative Transfer and Retrieval Tool. *Journal of*
797 *Quantitative Spectroscopy and Radiative Transfer*, 109(6):1136–1150, 2008.
798 doi: 10.1016/j.jqsrt.2007.11.006.

799 P. G. J. Irwin, N. Bowles, A. S. Braude, R. Garland, and S. Calcutt. Analysis
800 of Gaseous Ammonia ($NH_3$) Absorption in the Visible Spectrum of Jupiter.
801 *Icarus*, 302:426–436, 2018. doi: 10.1016/j.icarus.2017.11.031.

802 P. G. J. Irwin, N. Bowles, A. S. Braude, R. Garland, S. Calcutt, P. A. Coles, S. N.
803 Yurchenko, and J. Tennyson. Analysis of Gaseous Ammonia ($NH_3$) Absorption

in the Visible Spectrum of Jupiter - Update. *Icarus*, 321:572–582, 2019a. doi: 10.1016/j.icarus.2018.12.008.

P. G. J. Irwin, D. Toledo, A. S. Braude, R. Bacon, P. M. Weilbacher, N. A. Teanby, L. N. Fletcher, and G. S. Orton. Latitudinal Variation in the Abundance of Methane ($CH_4$) Above the Clouds in Neptune's Atmosphere from VLT/MUSE Narrow Field Mode Observations. *Icarus*, 331:69–82, 2019b.

E. Karkoschka. Spectrophotometry of the Jovian Planets and Titan at 300-to 1000-nm Wavelength [sic]: The Methane Spectrum. *Icarus*, 111:174–192, 1994. doi: 10.1006/icar.1994.1139.

E. Karkoschka. Methane, Ammonia, and Temperature Measurements of the Jovian Planets and Titan from CCD–Spectrophotometry. *Icarus*, 133:134–146, 1998. doi: 10.1006/icar.1998.5913.

E. Karkoschka and M. G. Tomasko. Methane Absorption Coefficients for the Jovian Planets from Laboratory, Huygens, and HST Data. *Icarus*, 205:674–694, 2010. doi: 10.1016/j.icarus.2009.07.044.

A. A. Lacis and V. Oinas. A Description of the Correlated K Distribution Method for Modeling Nongray Gaseous Absorption, Thermal Emission, and Multiple Scattering in Vertically Inhomogeneous Atmospheres. *Journal of Geophysical Research: Atmospheres*, 96:9027–9063, 1991. doi: 10.1029/90JD01945.

L. A. Lebofsky and M. B. Fegley. Laboratory Reflection Spectra for the Determination of Chemical Composition of Icy Bodies. *Icarus*, 28:379–387, 1976. doi: 10.1016/0019-1035(76)90151-2.

P. S. Lii, M. H. Wong, and I. de Pater. Temporal Variation of the Tropospheric Cloud and Haze in the Jovian Equatorial Zone. *Icarus*, 209:591–601, 2010.

M. J. Loeffler and R. L. Hudson. Coloring Jupiter's Clouds: Radiolysis of Ammonium Hydrosulfide ($NH_4SH$). *Icarus*, 302:418–425, 2018. doi: 10.1016/j.icarus.2017.10.041.

M. J. Loeffler, R. L. Hudson, N. J. Chanover, and A. A. Simon. Giant-Planet Chemistry: Ammonium Hydrosulfide ($NH_4SH$), its IR spectra and Thermal and Radiolytic Stabilities. *Icarus*, 258:181–191, 2015. doi: 10.1016/j.icarus.2015.06.015.

M. J. Loeffler, R. L. Hudson, N. J. Chanover, and A. A. Simon. The Spectrum of Jupiter's Great Red Spot: The Case for Ammonium Hydrosulfide ($NH_4SH$). *Icarus*, 271:265–268, 2016. doi: 10.1016/j.icarus.2016.02.010.

J. V. Martonchik, G. S. Orton, and J. F. Appleby. Optical Properties of $NH_3$ Ice from the Far Infrared to the Near Ultraviolet. *Applied Optics*, 23:541–547, 1984. doi: 10.1364/AO.23.000541.

K. I. Matcheva, B. J. Conrath, P. J. Gierasch, and F. M. Flasar. The Cloud Structure of the Jovian Atmosphere As Seen by the Cassini/CIRS Experiment. *Icarus*, 179:432–448, 2005. doi: 10.1016/j.icarus.2005.06.020.

W. McLean, D. M. Stam, S. Bagnulo, G. Borisov, M. Devogèle, A. Cellino, J. P. Rivet, P. Bendjoya, D. Vernet, G. Paolini, et al. A Polarimetric Investigation of Jupiter: Disk-Resolved Imaging Polarimetry and Spectropolarimetry. *Astronomy & Astrophysics*, 601:A142, 2017. doi: 10.1051/0004-6361/201629314.

I. Mendikoa, A. Sánchez-Lavega, S. Pérez-Hoyos, R. Hueso, J. F. Rojas, and J. López-Santiago. Temporal and Spatial Variations of the Absolute Reflectivity of Jupiter and Saturn from 0.38 to 1.7 $\mu$m with PlanetCam-UPV/EHU. *Astronomy & Astrophysics*, 607:A72, 2017. doi: 10.1051/0004-6361/201731109.

J. I. Moses, C. Visscher, T. C. Keane, and A. Sperier. On the Abundance of Non-Cometary HCN on Jupiter. *Faraday discussions*, 147:103–136, 2010. doi: 10.1039/c003954c.

K. Nassau. *The Physics and Chemistry of Color: The Fifteen Causes of Color*. Wiley series in pure and applied optics. Wiley, 1983. ISBN 0-471-86776-4.

H. B. Niemann, S. K. Atreya, G. R. Carignan, T. M. Donahue, J. A. Haberman, D. N. Harpold, R. E. Hartle, D. M. Hunten, W. T. Kasprzak, P. R. Mahaffy, et al. The Composition of the Jovian Atmosphere As Determined by the Galileo Probe Mass Spectrometer. *Journal of Geophysical Research: Planets*, 103: 22831–22846, 1998. doi: 10.1029/98JE01050.

I. Ordóñez-Etxeberria, R. Hueso, A. Sánchez-Lavega, and S. Pérez-Hoyos. Spatial Distribution of Jovian Clouds, Hazes and Colors from Cassini ISS Multi-Spectral Images. *Icarus*, 267:34–50, 2016. doi: 10.1016/j.icarus.2015.12.008.

T. Owen and R. J. Terrile. Colors on Jupiter. *Journal of Geophysical Research: Space Physics*, 86:8797–8814, 1981. doi: 10.1029/JA086iA10p08797.

C. Palotai, T. E. Dowling, and L. N. Fletcher. 3D Modeling of Interactions Between Jupiter's Ammonia Clouds and Large Anticyclones. *Icarus*, 232:141–156, 2014. doi: 10.1016/j.icarus.2014.01.005.

G. N. Plass, G. W. Kattawar, and F. E. Catchings. Matrix Operator Theory of Radiative Transfer. 1: Rayleigh Scattering. *Applied Optics*, 12:314–329, 1973. doi: 10.1364/AO.12.000314.

B. Ragent, D. S. Colburn, K. A. Rages, T. C. D. Knight, P. Avrin, G. S. Orton, P. A. Yanamandra-Fisher, and G. W. Grams. The Clouds of Jupiter: Results of the Galileo Jupiter Mission Probe Nephelometer Experiment. *Journal of Geophysical Research: Planets*, 103:22891–22909, 1998. doi: 10.1029/98JE00353.

J. T. Rayner, D. W. Toomey, P. M. Onaka, A. J. Denault, W. E. Stahlberger, W. D. Vacca, M. C. Cushing, and S. Wang. SpeX: A Medium-Resolution 0.8-5.5 Micron Spectrograph and Imager for the NASA Infrared Telescope Facility. *Publications of the Astronomical Society of the Pacific*, 115:362, 2003. doi: 10.1086/367745.

C. D. Rodgers. Information Content and Optimization of High-Spectral-Resolution Measurements. In *SPIE's 1996 International Symposium on Optical Science, Engineering, and Instrumentation*, pages 136–147. International Society for Optics and Photonics, 1996.

C. D. Rodgers. *Inverse Methods for Atmospheric Sounding: Theory and Practice*, volume 2. World Scientific, 2000.

J. H. Rogers. *The Giant Planet Jupiter*. Cambridge University Press, 1995.

C. Romanescu, J. Marschall, D. Kim, A. Khatiwada, and K. S. Kalogerakis. Refractive Index Measurements of Ammonia and Hydrocarbon Ices at 632.8 nm. *Icarus*, 205:695–701, 2010. doi: 10.1016/j.icarus.2009.08.016.

L. S. Rothman, I. E. Gordon, Y. Babikov, A. Barbe, D. C. Benner, P. F. Bernath, M. Birk, L. Bizzocchi, V. Boudon, L. R. Brown, et al. The HITRAN2012 Molecular Spectroscopic Database. *Journal of Quantitative Spectroscopy and Radiative Transfer*, 130:4–50, 2013. doi: 10.1016/j.jqsrt.2013.07.002.

A. Sánchez-Lavega, J. H. Rogers, G. S. Orton, E. García-Melendo, J. Legarreta, F. Colas, J. L. Dauvergne, R. Hueso, J. F. Rojas, S. Pérez-Hoyos, et al. A Planetary-Scale Disturbance in the Most Intense Jovian Atmospheric Jet from JunoCam and Ground-Based Observations. *Geophysical Research Letters*, 44: 4679–4686, 2017. doi: 10.1002/2017GL073421.

T. M. Sato, T. Satoh, and Y. Kasaba. Retrieval of Jovian Cloud Structure from the Cassini ISS Limb-Darkening Data: I. Continuum Scattering Phase Functions for Cloud and Haze in the South Tropical Zone. *Icarus*, 222:100–121, 2013. doi: 10.1016/j.icarus.2012.09.035.

M. A. Satorre, J. Leliwa-Kopystynski, C. Santonja, and R. Luna. Refractive Index and Density of Ammonia Ice at Different Temperatures of Deposition. *Icarus*, 225:703–708, 2013. doi: 10.1016/j.icarus.2013.04.023.

A. A. Simon, M. H. Wong, J. H. Rogers, G. S. Orton, I. De Pater, X. Asay-Davis, R. W. Carlson, and P. S. Marcus. Dramatic Change in Jupiter's Great Red Spot from Spacecraft Observations. *The Astrophysical Journal Letters*, 797:L31, 2014. doi: 10.1088/2041-8205/797/2/L31.

A. A. Simon, M. H. Wong, and G. S. Orton. First Results from the Hubble OPAL Program: Jupiter in 2015. *The Astrophysical Journal*, 812:55, 2015. doi: 10.1088/0004-637X/812/1/55.

A. A. Simon, F. Tabataba-Vakili, R. Cosentino, R. F. Beebe, M. H. Wong, and G. S. Orton. Historical and Contemporary Trends in the Size, Drift, and Color of Jupiter's Great Red Spot. *The Astronomical Journal*, 155:151, 2018. doi: 10.3847/1538-3881/aaae01.

A. A. Simon-Miller, D. Banfield, and P. J. Gierasch. Color and the Vertical Structure in Jupiter's Belts, Zones, and Weather Systems. *Icarus*, 154:459–474, 2001. doi: 10.1006/icar.2001.6742.

L. A. Sromovsky and P. M. Fry. Jupiter's Cloud Structure As Constrained By Galileo Probe And HST Observations. *Icarus*, 157:373–400, 2002. doi: 10.1006/icar.2002.6844.

L. A. Sromovsky, K. H. Baines, P. M. Fry, and R. W. Carlson. A Possibly Universal Red Chromophore for Modeling Color Variations on Jupiter. *Icarus*, 291: 232–244, 2017. doi: 10.1016/j.icarus.2016.12.014.

C. P. Stoll. *Polarimetry of Jupiter at Large Phase Angles*. PhD thesis, Arizona Univ., Tucson., 1980.

P. D. Strycker, N. J. Chanover, A. A. Simon-Miller, D. Banfield, and P. J. Gierasch. Jovian Chromophore Characteristics from Multispectral HST Images. *Icarus*, 215:552–583, 2011. doi: 10.1016/j.icarus.2011.08.004.

W. R. Thompson. Global Four-Band Spectral Classification of Jupiter's Clouds: Color/Albedo Units and Trends. *The International Journal of Supercomputing Applications*, 4:48–65, 1990. doi: 10.1177/109434209000400205.

L. Ventress and A. Dudhia. Improving the Selection of IASI Channels for Use in Numerical Weather Prediction. *Quarterly Journal of the Royal Meteorological Society*, 140(684):2111–2118, 2014. doi: 10.1002/qj.2280.

U. von Zahn, D. M. Hunten, and G. Lehmacher. Helium in Jupiter's Atmosphere: Results from the Galileo Probe Helium Interferometer Experiment. *Journal of Geophysical Research: Planets*, 103:22815–22830, 1998. doi: 10.1029/98JE00695.

P. M. Weilbacher, O. Streicher, T. Urrutia, A. Pécontal-Rousset, A. Jarno, and R. Bacon. The MUSE Data Reduction Pipeline: Status after Preliminary Acceptance Europe. In N. Manset and P. Forshay, editors, *Astronomical Data Analysis Software and Systems XXIII*, volume 485 of *Astronomical Society of the Pacific Conference Series*, page 451, 2014.

R. A. West, K. H. Baines, A. J. Friedson, D. Banfield, B. Ragent, and F. W. Taylor.

949 Jovian Clouds and Haze. In *Jupiter: The Planet, Satellites, and Magnetosphere*.
950 Cambridge University Press, 2004.

951 L. C. Zuchowski, Y. H. Yamazaki, and P. L. Read. Modeling Jupiter's Cloud
952 Bands and Decks. 2. Distribution and Motion of Condensates. *Icarus*, 200:
953 563–573, 2009. doi: 10.1016/j.icarus.2008.11.015.

| Observation ID | Seeing (arcsec) | Airmass | Sub-observer longitude (III) |
|---|---|---|---|
| 2014-02-17T02:07:56.907 | 0.64 | 1.500 | 18.92 |
| 2017-05-15T02:01:59.328 | 1.10 | 1.067 | 165.5 |
| 2018-04-09T06:04:06.918 | 0.36 | 1.028 | 121.14 |

**Table 1:** List of MUSE observations analysed in this work.

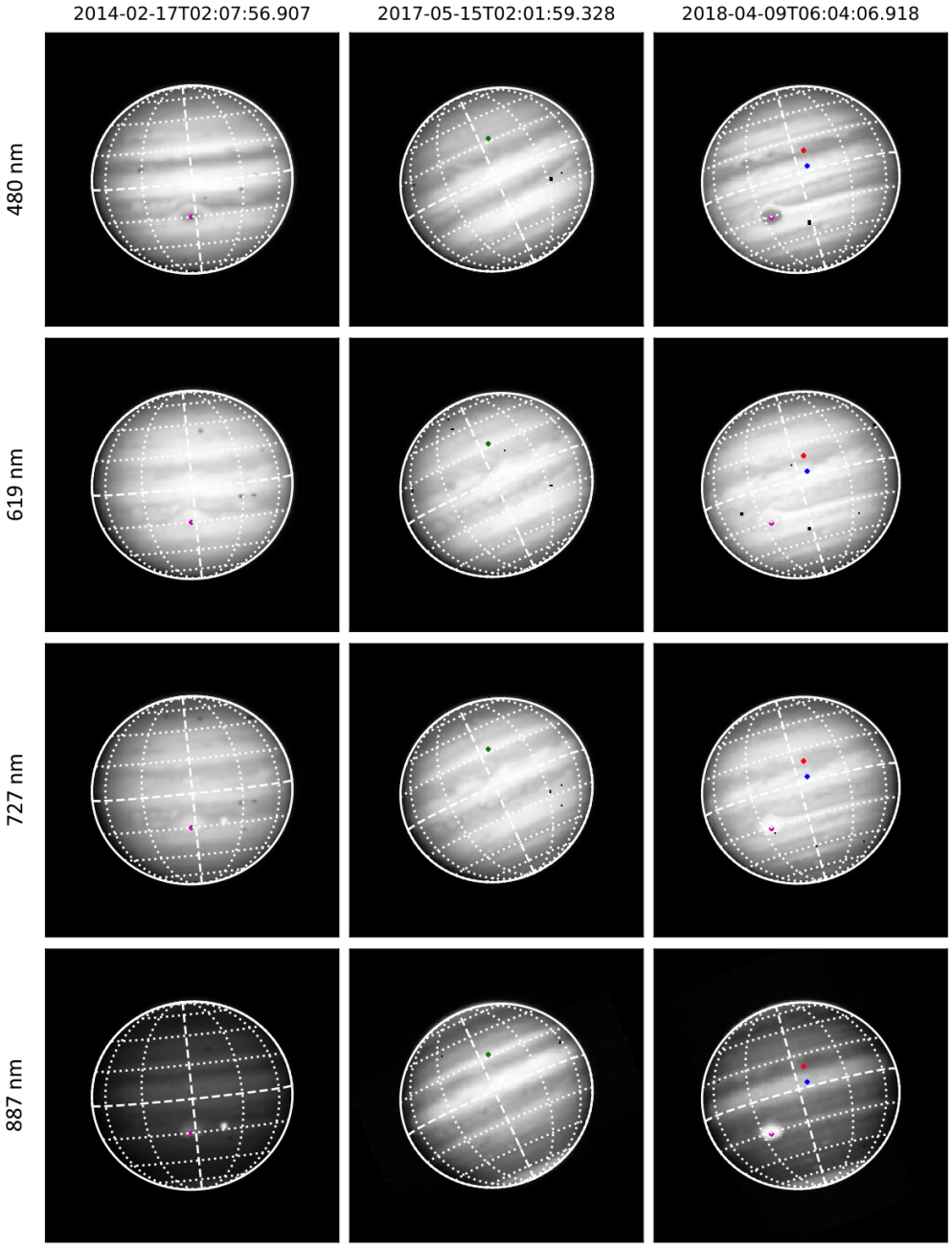


**Figure 1:** An image of each of the three MUSE observations of Jupiter at four sample wavelengths: 480 nm (sensitive to variations in chromophore), 619 nm (sensitive to variations in the deepest visible cloud layers, around 1-2 bars), 727 nm (sensitive to variations in upper tropospheric haze around 0.3-0.5 bars) and 887 nm (sensitive to the highest observable haze layers in the MUSE wavelength range, around 0.2-0.3 bars). In each case, the thick white line indicates the calculated terminator of Jupiter through ellipsoid limb fitting, the white dashed lines indicate the equator and central meridian (refer to Table 1 for the System III longitude in each case) and the white dotted lines indicate lines of planetocentric latitude (in $20^o$ intervals) and longitude (in $30^o$ intervals from the central meridian). Locations of sample spectra from the EZ (in blue), the NEB (in red), the NTBs (in green) and the GRS (in purple) are marked in each image. The bright white spot that is visible in the 2014 image around $20^o$ eastwards of the GRS is Europa.

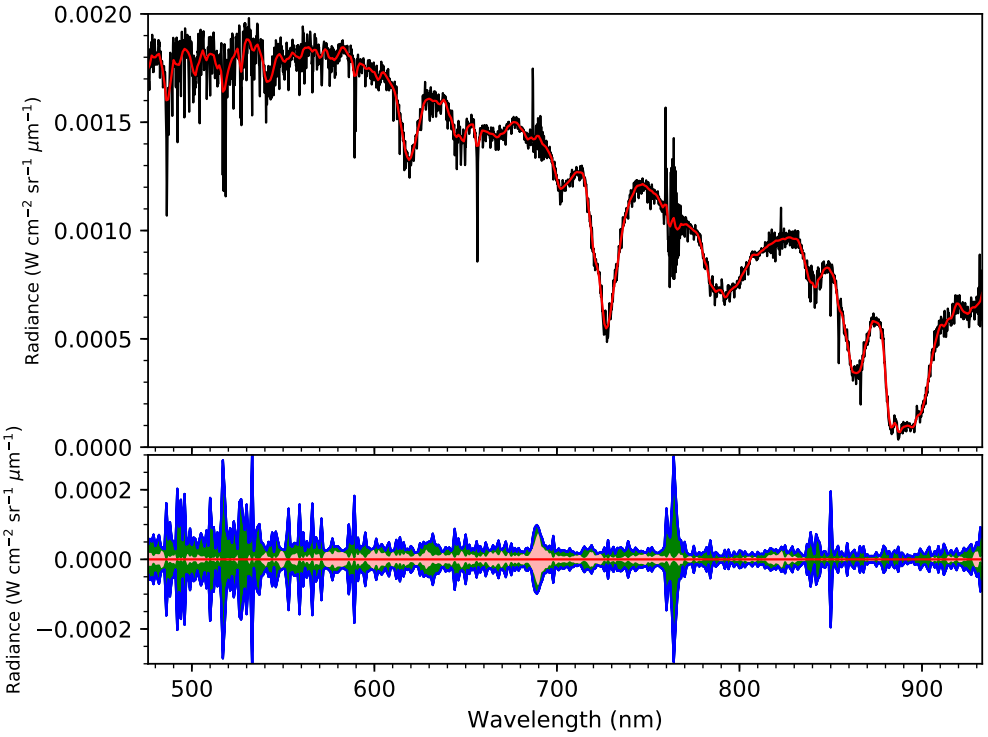


**Figure 2:** Top panel: A sample spectrum of the EZ (black) at native resolution and (red) following smoothing to 1 nm resolution. Bottom panel: spectral uncertainties associated with the smoothed EZ spectrum. In light red is the spectral uncertainty contribution from the errors calculated by the ESOREX pipeline following the smoothing process, taking into account spectral correlation. However, this is seen to underestimate the spectral error at certain wavelengths, notably in regions of telluric noise (e.g. 760 nm) and in regions where a large number of solar spectral lines are present (e.g. 500-540 nm). For this reason, we add an extra bias term (in green) to compensate for oversmoothing of the spectrum. On top of this we include an additional 1% uncertainty (in blue) to account for forward modelling error.

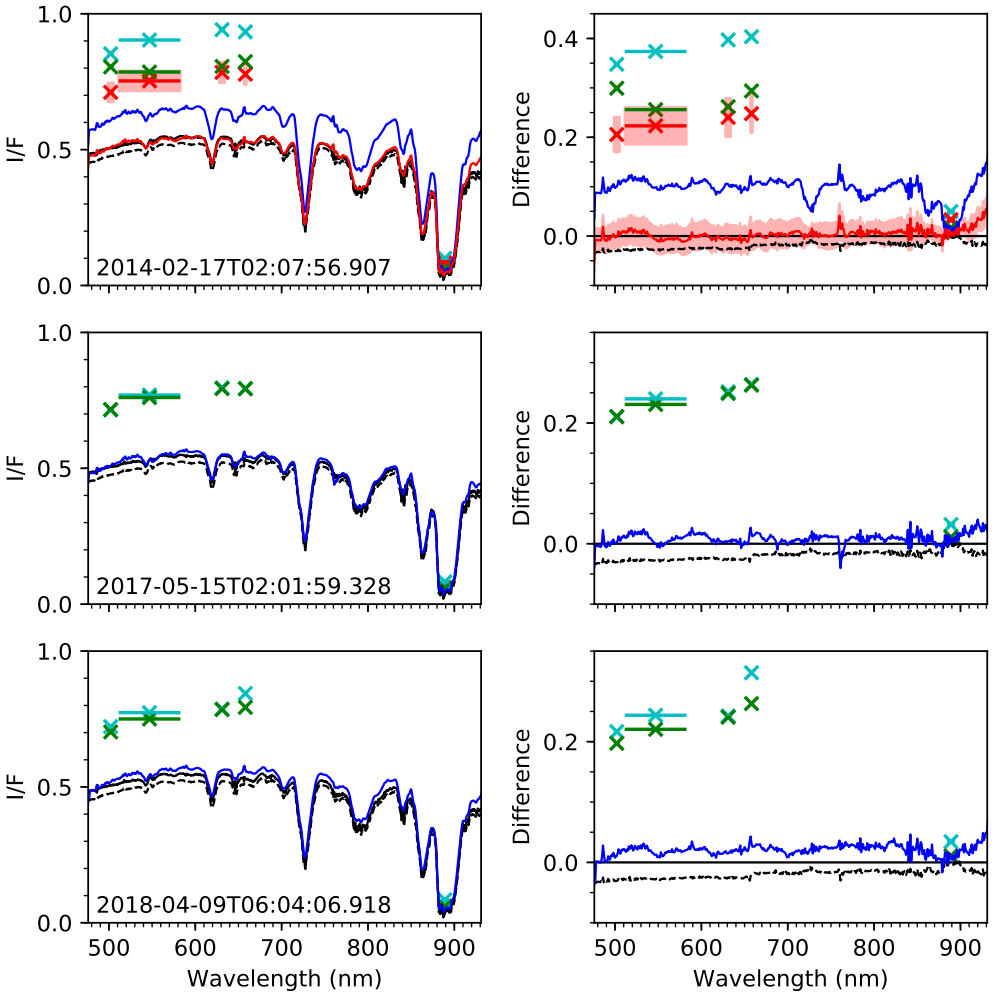


**Figure 3:** Verification of calibration of MUSE I/F values against both the disc-averaged spectra of Karkoschka (1994) (black, dashed) and Karkoschka (1998) (black, solid), and against global HST/WFC3 observations obtained closest in time (from top to bottom: 19th of January 2015, 3rd of April 2017, 17th of April 2018) to the corresponding MUSE observation as part of the OPAL programme (Simon et al., 2015). The MUSE observation timestamp in each case is given in the bottom-left corner of each plot, and the disc-average of each MUSE dataset shown in dark blue. For cross-calibration with the HST/WFC3 observations (green crosses), each MUSE observation was first multiplied by five UVIS2 HST/WFC3 wavelength filter functions (F502N, F547M, F631N, F658N and FQ889N) and a Minnaert correction applied through empirical calculation of limb-darkening over single zonal swaths. The latitudinal average was then calculated as stated in the text, and is shown as light blue crosses on the diagram (the horizontal lines indicate the FWHM of each of the HST filter functions). We show that the calibration of the MUSE data from 2017 and 2018 is mostly in keeping with both the Karkoschka (1998) data and the HST/WFC3 data, both in terms of the shape of the spectrum and in the absolute calculation of I/F. However, the MUSE data from 2014 has to be scaled downwards by 20% over all wavelengths (the scaled disc-averaged spectrum shown in red, with 5% uncertainties shaded) in order to be within 5% of the Karkoschka and HST/WFC3 data.

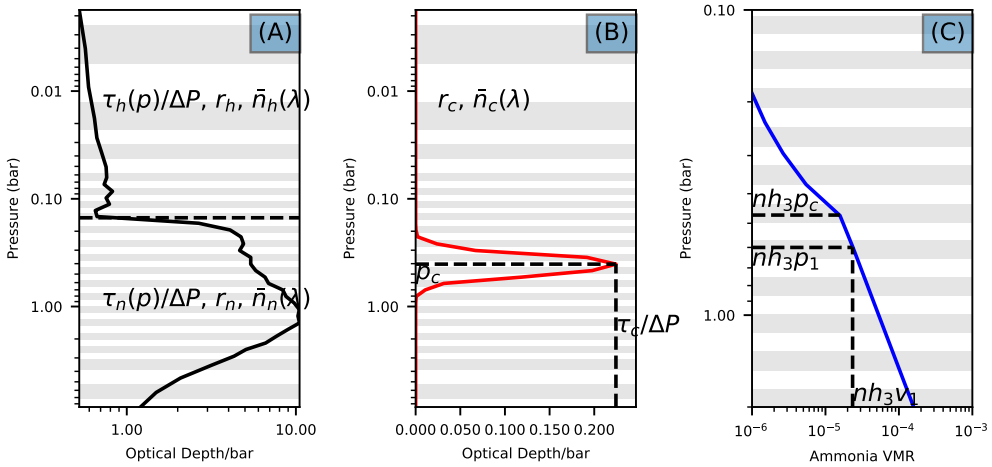


**Figure 4:** Illustration of the cloud model used in this work, showing a retrieved profile from spectral limb-darkening of the NEB when $n_n = 1.42$, $r_n = 1\mu m$ and $r_c = 0.05\mu m$. Plot (A) shows conservatively-scattering aerosol retrieved continuously over the entire vertical extent of the atmosphere. For pressure levels deeper than 0.15 bars, the aerosol is assumed to be 'cloud', characterised by an optical depth per bar (that is, the optical depth divided by the pressure interval $\Delta p$ of the homogeneous layer in question) as a function of pressure $\tau_n(p)/\Delta p$ (with correlation length 1.5), size distribution following a Gamma distribution of effective radius $r_n$ and variance 0.05, and complex refractive index as a function of wavelength $\bar{n}_n(\lambda) = n_n(\lambda) + ik_n(\lambda)$, where $k_n(\lambda)$ is assumed close to zero for all wavelengths and is parametrised with a correlation length of 0.1. For pressure levels shallower than 0.15 bars, the aerosol is assumed to be 'haze' and parametrised analogously using the variables $\tau_h(p)/\Delta p$, $r_h$ and $n_h(\lambda)$. Plot (B) shows chromophore abundance retrieved as a Gaussian profile, of peak optical depth per bar $\tau_c/\Delta p$ at pressure level $p_c$ independently retrieved and with a FWHM of a quarter of a pressure scale height, and with $r_c$ and $\bar{n}_c(\lambda) = n_c(\lambda) + ik_c(\lambda)$ parametrised analogously to conservatively-scattering aerosol. Plot (C) shows the gaseous ammonia profile with two parameters independently retrieved: a volume mixing ratio value $nh_3v_1$ at a reference pressure level $nh_3p_1 = 0.6$ bars, and an exponentional fractional scale height $fsh$ retrieved between the bottom of the atmosphere and the condensation level $nh_3p_c$, pressures shallower than which ammonia is assumed saturated in the atmosphere (note that plot C is on a different pressure scale than plots A and B as we are only sensitive to ammonia abundances over a very small vertical range and the abundance declines very rapidly with height above the saturation level). We have also shaded in the homogeneous layers of the reference atmosphere in alternating white and grey horizontal bands.

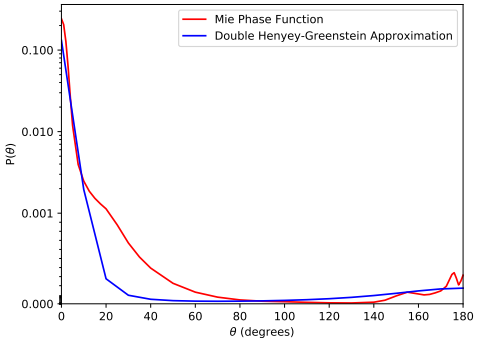


**Figure 5:** Example normalised Mie phase function (for a conservatively-scattering particle of radius 4μm) at a wavelength of 700 nm, compared to the equivalent 'smoothed' phase function computed using the double Henyey-Greenstein approximation.

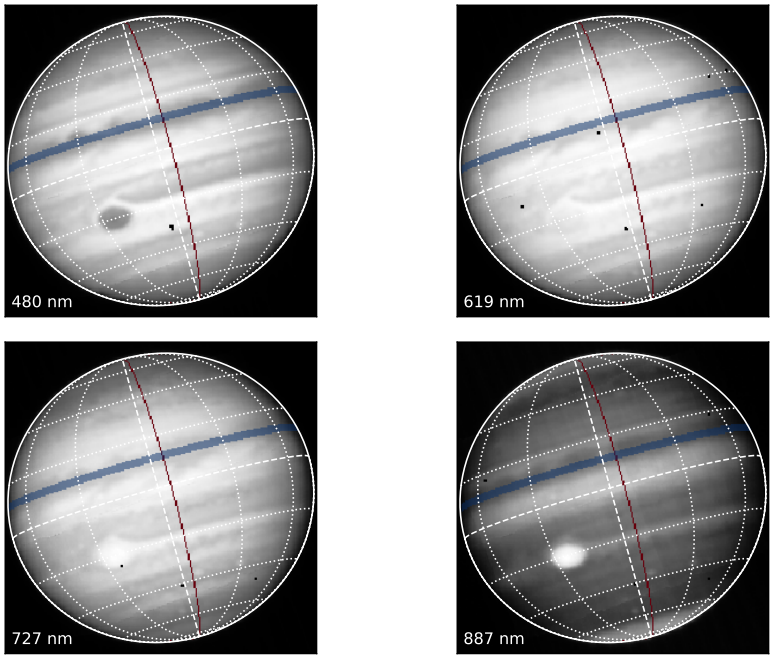


**Figure 6:** VLT/MUSE observation of Jupiter (timestamp 2018-04-09T06:04:06.918) shown at four individual wavelengths, with the limb-darkening swath in section 4.1 marked in blue and the vertical swath in section 5.2 marked in red. The key to the white gridlines is as in Figure 1. We have cropped out regions of sky observed by MUSE in these images in order to make the spatial resolution of Jupiter's surface by MUSE clearer to the reader. Note in particular the GRS at the bottom left, which is dark at wavelengths sensitive to chromophore but bright at wavelengths sensitive to cloud and haze, as well as the presence of a planetary wave in the northern NEB which is visible at all wavelengths.

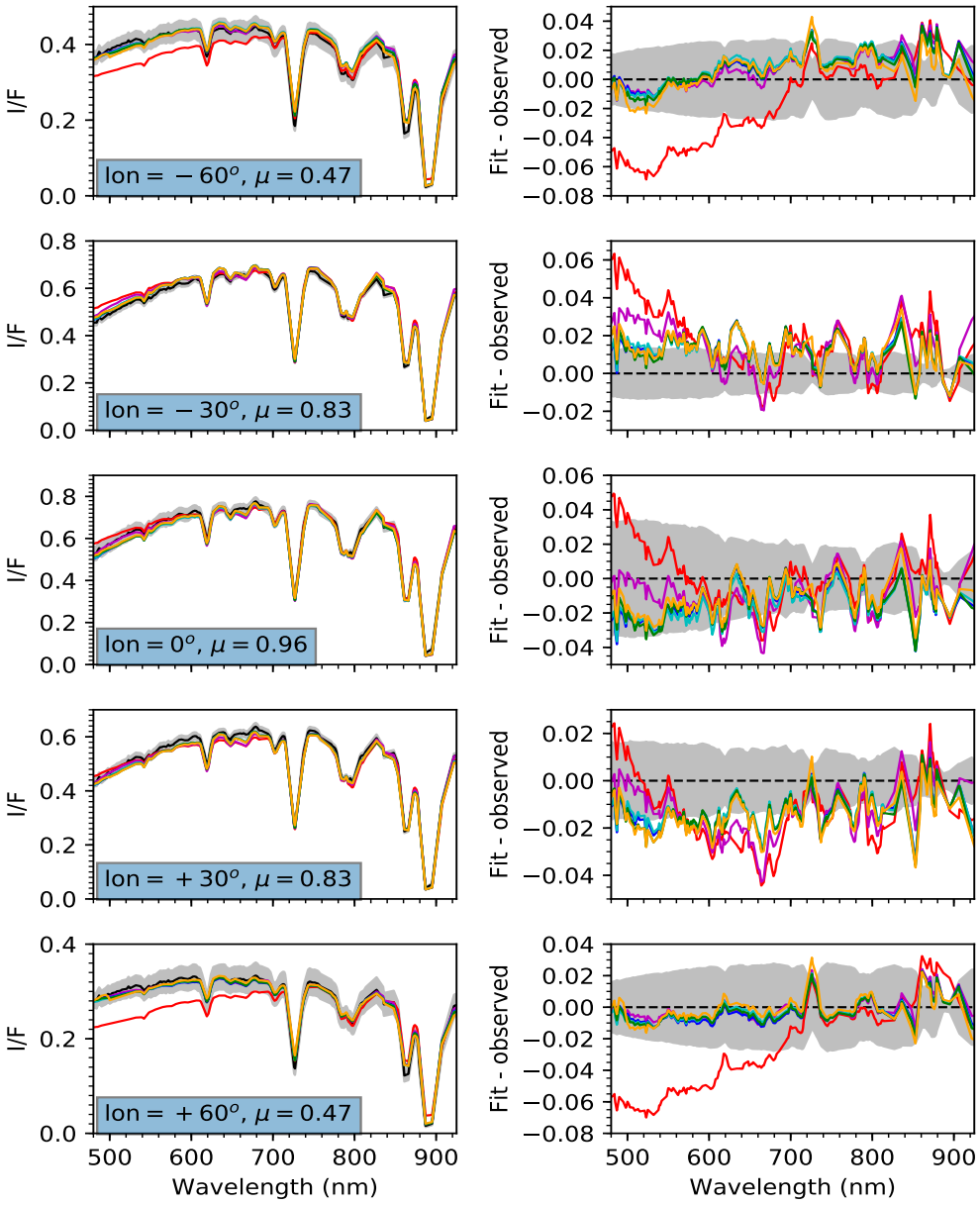


**Figure 7:** Spectral fit to the NEB at five different viewing geometries, comparing the fit to the observed spectra (in black, with uncertainties shaded in grey) using six different chromophore models. In red is the fit using the *Crème Brûlée* model (Sromovsky et al., 2017; Baines et al., 2019) with the chromophore optical constants of Carlson et al. (2016) ($\chi^2/n$ = 3.22). We can see that this fails to fit the blue-absorption gradient of the spectrum of the NEB, underestimating the slope at the shortest wavelengths at low viewing angles while overestimating the slope at green wavelengths at high viewing angles. By contrast, if we use our own model, but fix $k_c(\lambda)$ to the optical constants of Carlson et al. (2016), we get a much better fit. In this particular case, shown in purple, we get the best convergence when $n_n$ = 1.42, $r_c$ = 0.1$\mu m$ and $r_n$ = 1$\mu m$ ($\chi^2/n$ = 1.48). Nonetheless, we can still improve on this fit. The remaining fits use the best optical constant solutions that were retrieved directly from the spectra, in three cases where $r_n$ = 1$\mu m$, $n_n$ = 1.42 and $r_c$ was fixed to 0.05 μm (light blue, $\chi^2/n$ = 1.13), 0.2 μm (dark blue, $\chi^2/n$ = 1.14), and 0.5 μm (green, $\chi^2/n$ = 1.15) respectively, plus one case where $n_n$ = 1.5, $r_n$ = 0.75$\mu m$ and $r_c$ = 0.5$\mu m$ (orange, $\chi^2/n$ = 1.17). All three solutions give a reasonable fit to each of the five viewing geometries but are relatively indistinguishable in quality given the spectral uncertainties involved.

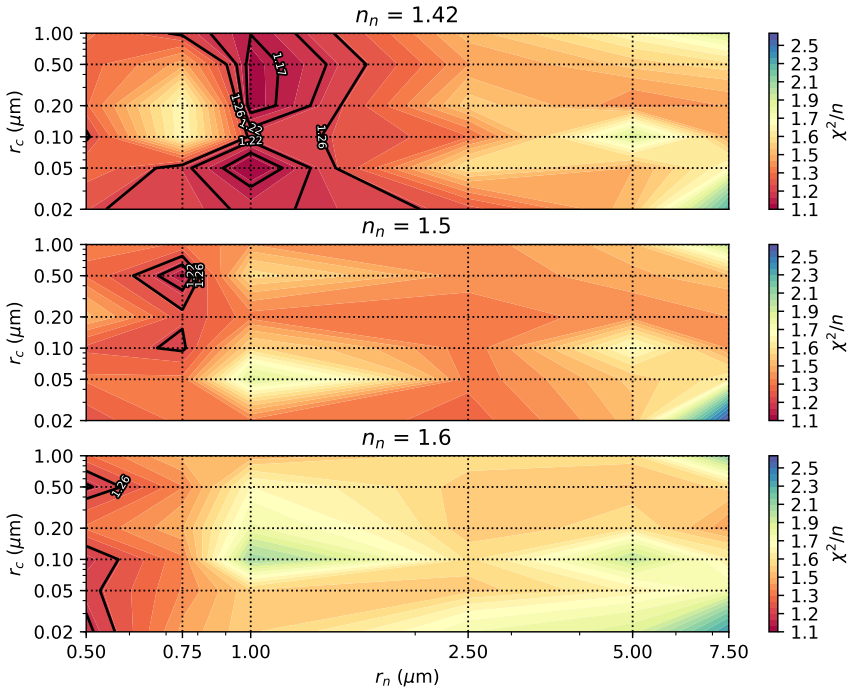


**Figure 8:** A map of the 'goodness of fit' ($\chi^2/n$) values obtained through limb-darkening analysis of the NEB, as a function of the effective radius of cloud ($r_n$) and chromophore ($r_c$) particles, as well as the real part of the refractive index $n_n$ of the cloud particles. Individual values of prior $r_n$ and $r_c$ used in our retrievals are marked at the intersections of each of the vertical and horizontal black lines, and the resulting contours interpolated from those points. Dark red colours indicate a better quality of fit in each case. The lowest $\chi^2/n$ value we were able to retrieve was equal to 1.12, and the solid black lines give the $\chi^2/n$ values within a 1-, 2- and 3-sigma uncertainty interval respectively around this minimum value. In general, for each value of $n_n$, the optimal solutions tend to cluster at a given value of $r_n$ but for which a wide range of $r_c$ values are possible. Raising the value of $n_n$ tends to lower this optimal value of $r_n$. However, two local minima in $\chi^2/n$ are clearly present in the $n_n = 1.42$ case that are not as profound for higher values of $n_n$. This provides some evidence that the deepest cloud layers observable at visible and near-infrared wavelengths have a low real refractive index value.

| **Profile** | **Variable definition** | **Variable symbol** | **Fixed (F) or variable (V)?** | **Constraints where applicable** |
|---|---|---|---|---|
| Cloud (P>0.15 bars), haze (P<0.15 bars) | Aerosol abundance (optical depth/bar at 890 nm) as a function of pressure $P$ (in bars) | $\frac{\tau_n(P)}{\Delta p}$, $\frac{\tau_h(P)}{\Delta p}$ | V | |
| | Correlation length of aerosol profile | $\Lambda_{\tau n}$, $\Lambda_{\tau h}$ | F | 1.5 |
| | Variance of particle size distribution | $\sigma_n$, $\sigma_h$ | | 0.05 |
| | Real refractive index (cloud) at $\lambda = 700nm$ | $n_n$ | | Found through $\chi^2/n$ analysis |
| | Real refractive index (haze) at $\lambda = 700nm$ | $n_h$ | | 1.4 |
| | Imaginary part of complex refractive index spectrum as a function of wavelength $\lambda$ | $k_n(\lambda)$, $k_h(\lambda)$ | | $10^{-9}\forall\lambda$ |
| | Correlation length of refractive index spectrum | $\Lambda_{kn}$, $\Lambda_{kh}$ | | 0.1 |
| | Effective cloud particle radius (μm) | $r_n$ | V* | Found through $\chi^2/n$ analysis |
| | Effective haze particle radius (μm) | $r_h$ | F* | $r_h < r_n$ |
| Chromophore | Aerosol abundance at centre of Gaussian (optical depth/bar at 890 nm) | $\frac{\tau_c(P)}{\Delta p}$ | V | |
| | Altitude of centre of Gaussian (bars) | $P_c$ | | |
| | Gaussian FWHM (pressure scale height) | $\Delta_c$ | F | 0.25 |
| | Effective particle radius (μm) | $r_c$ | | Found through $\chi^2/n$ analysis |
| | Variance of particle size distribution | $\sigma_c$ | | 0.1 |
| | Real refractive index at $\lambda = 700nm$ | $n_c$ | | 1.4 |
| | Correlation length of refractive index spectrum | $\Lambda_{kc}$ | | 0.1 |
| | Imaginary part of complex refractive index spectrum as a function of wavelength $\lambda$ | $k_c(\lambda)$ | F* | |
| Ammonia gas | Reference pressure level (bars) | $nh_3p_1$ | F | 0.6 |
| | Reference volume mixing ratio (VMR) at a pressure level of 0.6 bars | $nh_3v_1$ | V | Saturation-limited |
| | Fractional scale height | fsh | V | Saturation-limited, VMR must decrease with increasing altitude |

**Table 2:** Explanation of variables used to parametrise the forward model, with prior constraints specified when applicable. V* indicates variables that are fixed during limb-darkening analysis, but allowed to vary when doing point spectral retrievals. F* indicates variables that are allowed to vary during limb-darkening analysis, but fixed when doing point spectral retrievals to the values retrieved from limb-darkening.

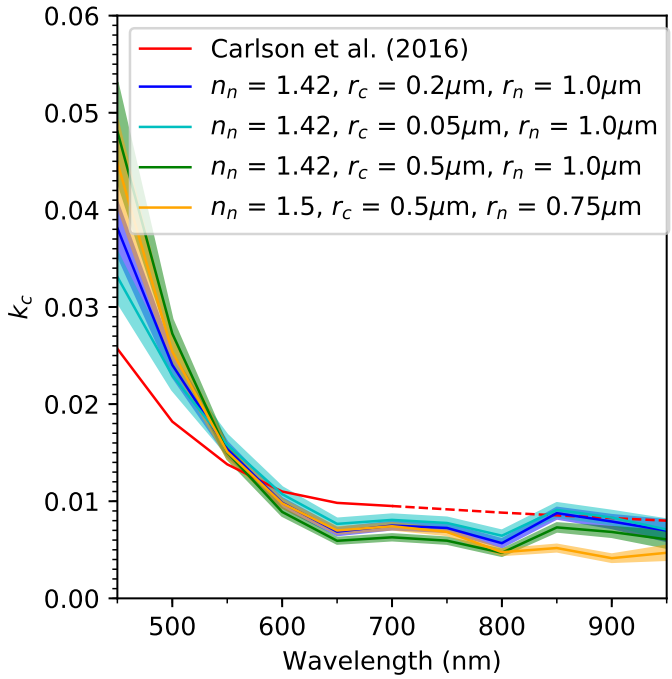


**Figure 9:** Chromophore imaginary refractive index solutions $k_c(\lambda)$ retrieved through limb-darkening analysis of the NEB (showing the four solutions with the best $\chi^2/n$ values) compared with the tabulated optical constants of Carlson et al. (2016), with the legend as in Figure 7 with uncertainties shaded. We can see that the general shape of the retrieved solutions of $k_c(\lambda)$ is relatively invariant regardless of $r_c$, with only minor modifications needed to the spectral slope.

| $n_n$ | 1.42 | | | 1.5 |
|---|---|---|---|---|
| $r_c$ (μm) | 0.05 | 0.2 | 0.5 | |
| $r_n$ (μm) | 1 | | | 0.75 |
| Wavelength (nm) | $k_c$ | | | |
| 450 | 0.033 ± 0.003 | 0.038 ± 0.003 | 0.048 ± 0.005 | 0.045 ± 0.004 |
| 500 | 0.023 ± 0.001 | 0.024 ± 0.001 | 0.027 ± 0.001 | 0.025 ± 0.001 |
| 550 | 0.016 ± 0.001 | 0.0154 ± 0.0007 | 0.0150 ± 0.0007 | 0.0151 ± 0.0006 |
| 600 | 0.0107 ± 0.0007 | 0.0098 ± 0.0004 | 0.0089 ± 0.0004 | 0.0098 ± 0.0004 |
| 650 | 0.0077 ± 0.0005 | 0.0069 ± 0.0003 | 0.0059 ± 0.0003 | 0.0070 ± 0.0003 |
| 700 | 0.0081 ± 0.0005 | 0.0075 ± 0.0005 | 0.0063 ± 0.0003 | 0.0074 ± 0.0003 |
| 750 | 0.0078 ± 0.0005 | 0.0072 ± 0.0004 | 0.0059 ± 0.0003 | 0.0068 ± 0.0003 |
| 800 | 0.0065 ± 0.0005 | 0.0057 ± 0.0004 | 0.0047 ± 0.0003 | 0.0048 ± 0.0003 |
| 850 | 0.0091 ± 0.0007 | 0.0088 ± 0.0005 | 0.0073 ± 0.0004 | 0.0052 ± 0.0003 |
| 900 | 0.0083 ± 0.0007 | 0.0079 ± 0.0007 | 0.0068 ± 0.0005 | 0.0041 ± 0.0004 |
| 950 | 0.007 ± 0.001 | 0.007 ± 0.001 | 0.0061 ± 0.0008 | 0.0047 ± 0.0007 |

**Table 3:** Tabulated retrieved imaginary refractive index spectra as shown in Figure 9.

| Retrieval from limb-darkening | | | | | | Application to GRS | | | | | | | |
|---|---|---|---|---|---|---|---|---|---|---|---|---|---|
| $\sigma$ | $n_n$ | $r_c$ (μm) | $r_n$ (μm) | $r_h$ (μm) | $\chi^2/n$ | $r_n$ (μm) | $\chi^2/n$ | Max. cloud+haze optical depth/bar | Max. chromophore optical depth/bar | Max. cloud+haze density (g/l) | Max. chromophore density (g/l) | Total cloud+haze column abundance (g/cm$^2$) | Total chromophore column abundance (g/cm$^2$) |
| 1 | **1.42** | **0.05** | **1** | **0.47 ± 0.03** | **1.12622** | **6.58 ± 0.05** | **0.663071** | **11.2 ± 0.7** | **1.03 ± 0.02** | **$(1.7 \pm 0.1) \times 10^{-6}$** | **$(6.6 \pm 0.2) \times 10^{-8}$** | **$(9 \pm 1) \times 10^{-3}$** | **$(6.3 \pm 0.3) \times 10^{-5}$** |
| | 1.42 | 0.2 | 1 | 0.48 ± 0.02 | 1.14259 | 7.62 ± 0.01 | 1.08430 | 21 ± 2 | 5.3 ± 0.1 | $(5.9 \pm 0.6) \times 10^{-6}$ | $(3.15 \pm 0.07) \times 10^{-8}$ | $(2.8 \pm 0.6) \times 10^{-2}$ | $(3.1 \pm 0.1) \times 10^{-5}$ |
| | 1.42 | 0.5 | 1 | 0.48 ± 0.02 | 1.14848 | 7.831 ± 0.007 | 2.37468 | 49 ± 6 | 13.0 ± 0.5 | $(1.3 \pm 0.2) \times 10^{-5}$ | $(4.2 \pm 0.2) \times 10^{-8}$ | $(5 \pm 2) \times 10^{-2}$ | $(4.8 \pm 0.3) \times 10^{-5}$ |
| | 1.5 | 0.5 | 0.75 | 0.50 ± 0.01 | 1.16793 | 0.094 ± 0.004 | 2.47952 | 74 ± 15 | 13.5 ± 0.5 | $(8 \pm 2) \times 10^{-6}$ | $(2.5 \pm 0.9) \times 10^{-8}$ | $(3 \pm 1) \times 10^{-2}$ | $(2.3 \pm 0.1) \times 10^{-5}$ |
| 2 | 1.42 | 1 | 1 | 0.45 ± 0.03 | 1.17243 | 5.38 ± 0.05 | 1.43397 | 430 ± 70 | 15.6 ± 0.4 | $(8 \pm 2) \times 10^{-5}$ | $(6.9 \pm 0.2) \times 10^{-8}$ | $(3 \pm 1) \times 10^{-1}$ | $(6.2 \pm 0.2) \times 10^{-5}$ |
| | 1.6 | 0.02 | 0.5 | 0.183 ± 0.003 | 1.20119 | 0.89 ± 0.01 | 0.653765 | 8.7 ± 0.6 | 0.45 ± 0.02 | $(8.3 \pm 0.8) \times 10^{-8}$ | $(5.4 \pm 0.2) \times 10^{-8}$ | $(5.2 \pm 0.8) \times 10^{-4}$ | $(5.2 \pm 0.3) \times 10^{-5}$ |
| | 1.42 | 0.02 | 1 | 0.52 ± 0.03 | 1.20469 | 7.773 ± 0.008 | 1.06207 | 11.5 ± 0.9 | 1.5 ± 0.1 | $(1.6 \pm 0.2) \times 10^{-6}$ | $(1.13 \pm 0.08) \times 10^{-7}$ | $(1.2 \pm 0.2) \times 10^{-2}$ | $(1.0 \pm 0.1) \times 10^{-4}$ |
| | 1.6 | 0.5 | 0.5 | 0.183 ± 0.002 | 1.2062 | 1.07 ± 0.03 | 2.1343 | 8.8 ± 0.6 | 6.9 ± 0.7 | $(2.7 \pm 0.2) \times 10^{-7}$ | $(3.3 \pm 0.3) \times 10^{-8}$ | $(1.0 \pm 0.1) \times 10^{-3}$ | $(3.3 \pm 0.6) \times 10^{-5}$ |
| | 1.6 | 0.1 | 0.5 | 0.40 ± 0.06 | 1.2149 | 0.745 ± 0.008 | 0.850912 | 15 ± 1 | 1.91 ± 0.05 | $(1.5 \pm 0.1) \times 10^{-7}$ | $(3.9 \pm 0.1) \times 10^{-8}$ | $(9 \pm 2) \times 10^{-4}$ | $(3.5 \pm 0.2) \times 10^{-5}$ |
| 3 | 1.42 | 0.05 | 0.75 | 0.066 ± 0.002 | 1.22733 | 4.76 ± 0.04 | 0.865846 | 13.6 ± 0.9 | 0.84 ± 0.05 | $(1.0 \pm 0.1) \times 10^{-6}$ | $(4.5 \pm 0.3) \times 10^{-8}$ | $(6.5 \pm 0.9) \times 10^{-3}$ | $(4.4 \pm 0.4) \times 10^{-5}$ |
| | 1.42 | 0.1 | 1 | 0.40 ± 0.05 | 1.2375 | 5.28 ± 0.06 | 0.751611 | 11.4 ± 0.7 | 1.84 ± 0.05 | $(1.9 \pm 0.2) \times 10^{-6}$ | $(3.6 \pm 0.1) \times 10^{-8}$ | $(1.0 \pm 0.2) \times 10^{-2}$ | $(3.6 \pm 0.2) \times 10^{-5}$ |
| | 1.42 | 0.02 | 0.75 | 0.071 ± 0.002 | 1.23781 | 6.86 ± 0.04 | 1.14264 | 10.2 ± 0.8 | 0.77 ± 0.05 | $(7.4 \pm 0.6) \times 10^{-7}$ | $(5.3 \pm 0.3) \times 10^{-8}$ | $(6.0 \pm 0.8) \times 10^{-3}$ | $(4.9 \pm 0.4) \times 10^{-5}$ |
| | 1.42 | 1 | 0.75 | 0.071 ± 0.002 | 1.24142 | 4.74 ± 0.08 | 1.24856 | 46 ± 6 | 12.4 ± 0.5 | $(9 \pm 1) \times 10^{-6}$ | $(5.5 \pm 0.2) \times 10^{-8}$ | $(4 \pm 1) \times 10^{-2}$ | $(4.9 \pm 0.3) \times 10^{-5}$ |
| | 1.6 | 0.05 | 0.5 | 0.35 ± 0.05 | 1.24357 | 0.87 ± 0.02 | 0.926087 | 8.7 ± 0.8 | 0.69 ± 0.03 | $(6.2 \pm 0.8) \times 10^{-8}$ | $(5.2 \pm 0.2) \times 10^{-8}$ | $(6 \pm 1) \times 10^{-4}$ | $(4.7 \pm 0.4) \times 10^{-5}$ |
| | 1.42 | 0.1 | 0.5 | 0.065 ± 0.002 | 1.24681 | 0.118 ± 0.004 | 0.918502 | 16 ± 2 | 2.4 ± 0.1 | $(1.3 \pm 0.2) \times 10^{-6}$ | $(3.7 \pm 0.2) \times 10^{-8}$ | $(8 \pm 2) \times 10^{-3}$ | $(3.3 \pm 0.2) \times 10^{-5}$ |
| | 1.5 | 0.1 | 0.75 | 0.40 ± 0.02 | 1.24714 | 1.14 ± 0.02 | 2.78717 | 45 ± 5 | 1.68 ± 0.06 | $(1.5 \pm 0.1) \times 10^{-6}$ | $(3.5 \pm 0.1) \times 10^{-8}$ | $(4.4 \pm 0.8) \times 10^{-3}$ | $(3.5 \pm 0.2) \times 10^{-5}$ |

**Table 4:** Results of the retrieval and selection of our universal chromophore solution. For each row, the first six columns show the results of fitting to the NEB through limb-darkening for given values of $n_n$, $r_n$ and $r_c$, while the last eight columns then show the results when the solution for $k_c(\lambda)$ retrieved through limb-darkening is applied to the spectrum of the GRS from 2018 and $r_n$ allowed to vary from its prior value (but $n_n$ and $r_c$ remain fixed). The rows are sorted in ascending order of $\chi^2/n$, and within sets of 1- 2- and 3$\sigma$ of the lowest $\chi^2/n$ from limb-darkening analysis (where $\sigma = \sqrt{1/500} \approx 0.045$). For the GRS retrievals, $n = 435$ and so $\sigma = \sqrt{2/435} \approx 0.068$. The selected universal chromophore solution is highlighted in bold, due to its low $\chi^2/n$ value for both the NEB and the GRS.

| | **EZ** | **NEB** | **NTBs (2017)** | **GRS (2000), unnormalised** | **GRS (2000), normalised** | **GRS (2014)** | **GRS (2018)** |
|---|---|---|---|---|---|---|---|
| $\tau_n(P_{max})/\Delta p$ | 10.6 ± 0.6 | 6.1 ± 0.5 | 8.0 ± 0.5 | 3.7 ± 0.4 | 7.3 ± 0.8 | 12 ± 2 | 11.2 ± 0.7 |
| $P_{max}$ | 1.4 ± 0.1 | 1.07 ± 0.08 | 1.4 ± 0.1 | 1.4 ± 0.1 | 1.4 ± 0.1 | 1.4 ± 0.1 | 0.23 ± 0.02 |
| $\tau_c/\Delta p$ | 0.20 ± 0.07 | 0.22 ± 0.02 | 0.26 ± 0.06 | 0.16 ± 0.05 | 0.13 ± 0.02 | 0.54 ± 0.05 | 1.03 ± 0.02 |
| $P_c$ | 0.30 ± 0.02 | 0.61 ± 0.04 | 0.35 ± 0.03 | 0.93 ± 0.07 | 0.7 ± 0.1 | 0.23 ± 0.02 | 0.19 ± 0.02 |
| $r_n$ | 4.40 ± 0.05 | 1.5 ± 0.2 | 4.90 ± 0.03 | 1.3 ± 0.2 | 1.5 ± 0.4 | 1.8 ± 0.3 | 6.58 ± 0.04 |
| $\chi^2/n$ | 0.85 ± 0.07 | 0.54 ± 0.07 | 0.56 ± 0.07 | 1.7 ± 0.2 | 1.9 ± 0.2 | 0.40 ± 0.07 | 0.66 ± 0.07 |

**Table 5:** Retrieved parameters associated with the locations whose fits are shown in Figures 10 and 11. $P_{max}$ is the pressure level (in bars) at which the cloud optical depth per bar is greatest. For the GRS (2000) case, the number of wavelengths is 63 and for the other spectra it is 435.

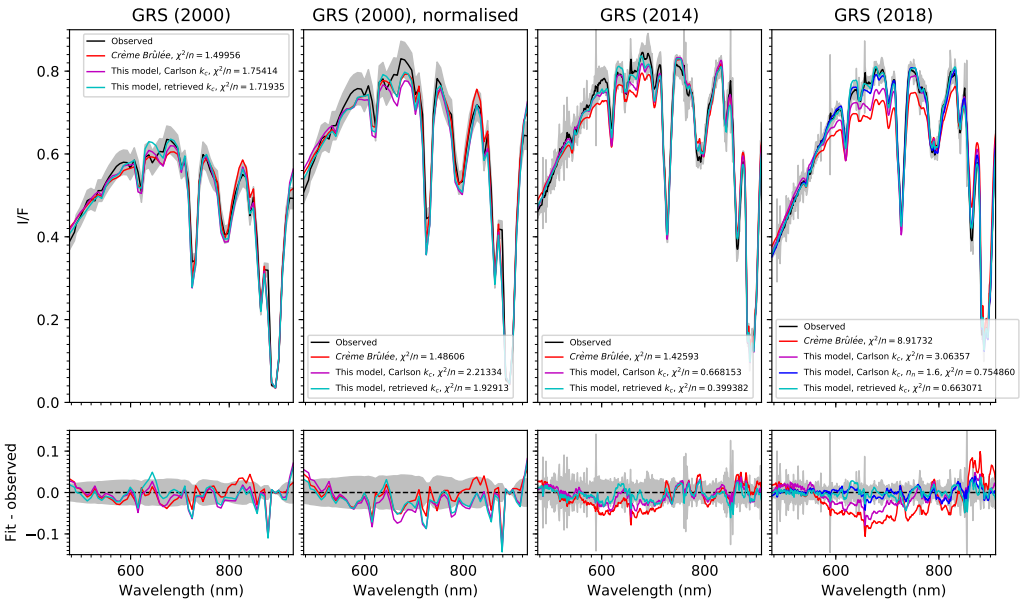


**Figure 10:** A comparison of the fit to the spectrum of the centre of the GRS obtained at different stages in its evolution: (left) in 2000, as obtained by Cassini/VIMS and provided in the supplementary data of Carlson et al. (2016); (second from left) the same spectrum, but normalised to an I/F value of 0.83 at 673 nm as suggested by Carlson et al. (2016) in order to be in line with contemporaneous observations of the GRS (although Sromovsky et al. (2017) suggest an intermediate scaling factor of 1.12 times the spectrum on the far left, based on comparisons of disc-averaged spectra of Jupiter); (second from right) in 2014, as obtained by VLT/MUSE before the simultaneous shrinking and reddening events described in Simon et al. (2014, 2018); and (right) in 2018, as obtained by VLT/MUSE after the shrinking and reddening of the GRS. In the case of the GRS (2000) spectra, we smoothed the methane k-tables and solar spectra to 7 nm resolution to be in keeping the VIMS-V spectral sampling before performing our retrievals. In each of the four cases, we compare the fits using the *Crème Brûlée* model in red, our own model but fixed to the optical constants of Carlson et al. (2016) in purple, and using our own model but with our own directly-retrieved optical constants in light blue (using the highlighted 'best-fit' values of $n_n$ and $r_c$ in Table 4). Although our retrieved optical constants provide a superior fit in all three cases, the fit using the *Crème Brûlée* model is still passable in 2000 and 2014 albeit with some discrepancy between 600 nm and 700 nm. This may explain the reasonable fits found by Sromovsky et al. (2017) and Baines et al. (2019) to VIMS spectra of the GRS using the *Crème Brûlée* model. By 2018, however, it is impossible to fit the spectrum of the GRS using the optical constants of Carlson et al. (2016), unless $r_n$ is raised to 1.6, which we show in dark blue ($r_c = 0.05\mu m$, $r_n = 5\mu m$). This clearly explains our motivation to retrieve our own chromophore solution.

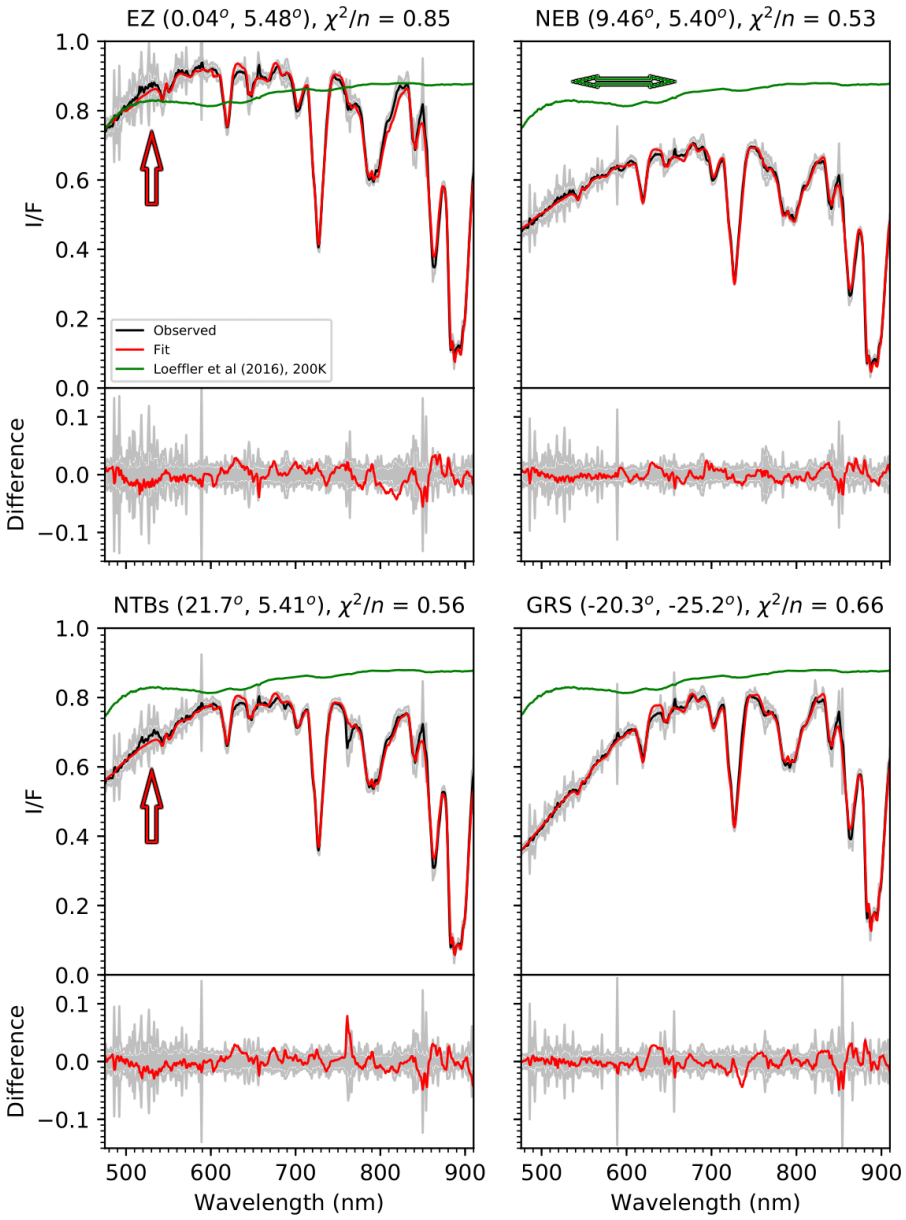


**Figure 11:** Fits to different representative MUSE spectra, using the 'universal chromophore' optical constants selected in section 4.2. The NTBs spectrum was obtained from MUSE dataset 2017-05-15T02:01:59.328 when the red colour of the NTBs was at its most prominent, while the remaining three spectra were obtained from dataset 2018-04-09T06:04:06.918 which was taken under the best observing conditions of all three datasets. For each of the four spectra, the given latitude values are planetocentric, while longitude values are east relative to the sub-observer. $\chi^2/n$ values of the quality of the fit of the retrieved imaginary refractive index spectrum to each MUSE spectrum are also shown. We have highlighted small deviations in the fit to the EZ and NTBs spectra at blue wavelengths with the red arrows, for which we have recommended further investigation (the apparent absorption feature present around 760 nm is due to telluric noise, which is particularly prominent in the NTBs spectrum as a consequence of imperfect airmass correction). For comparison, we also show the shape of the $NH_4SH$ absorption spectrum (in green, with the extent of the 600 nm absorption feature highlighted by the green arrow in the top-right diagram) as obtained by Loeffler et al. (2016) when reheated to 200K following proton irradiation, which clearly models the shape of Jovian spectra very poorly. Reference $NH_4SH$ absorption spectra obtained at lower temperatures have a similar shape to that at 200K, but with a much deeper 600 nm absorption feature that is non-existent in Jovian spectra.

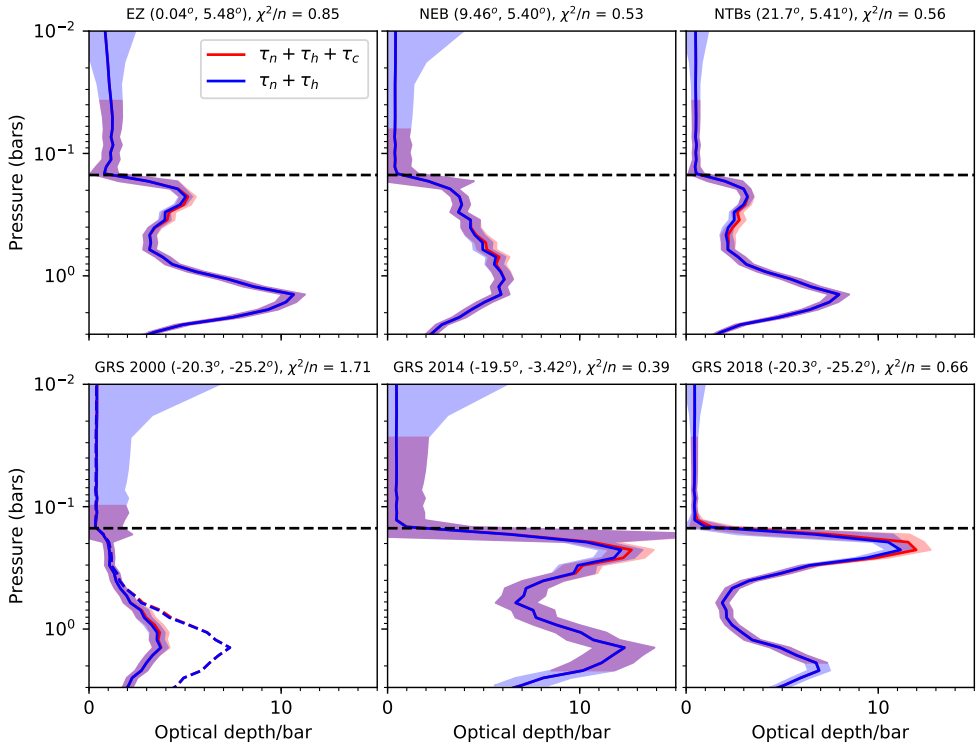


**Figure 12:** Retrieved cloud, chromophore and haze vertical profiles for the EZ, the NEB, the NTBs (in 2017) and the GRS from three different years, with errors shaded. The GRS (2000) solid profiles were retrieved using the unnormalised VIMS spectrum, with the dashed lines showing the results for the normalised spectrum. In each plot, the black dashed line shows the 0.15 bar cut-off between the $\tau_n$ and $\tau_h$ profiles.

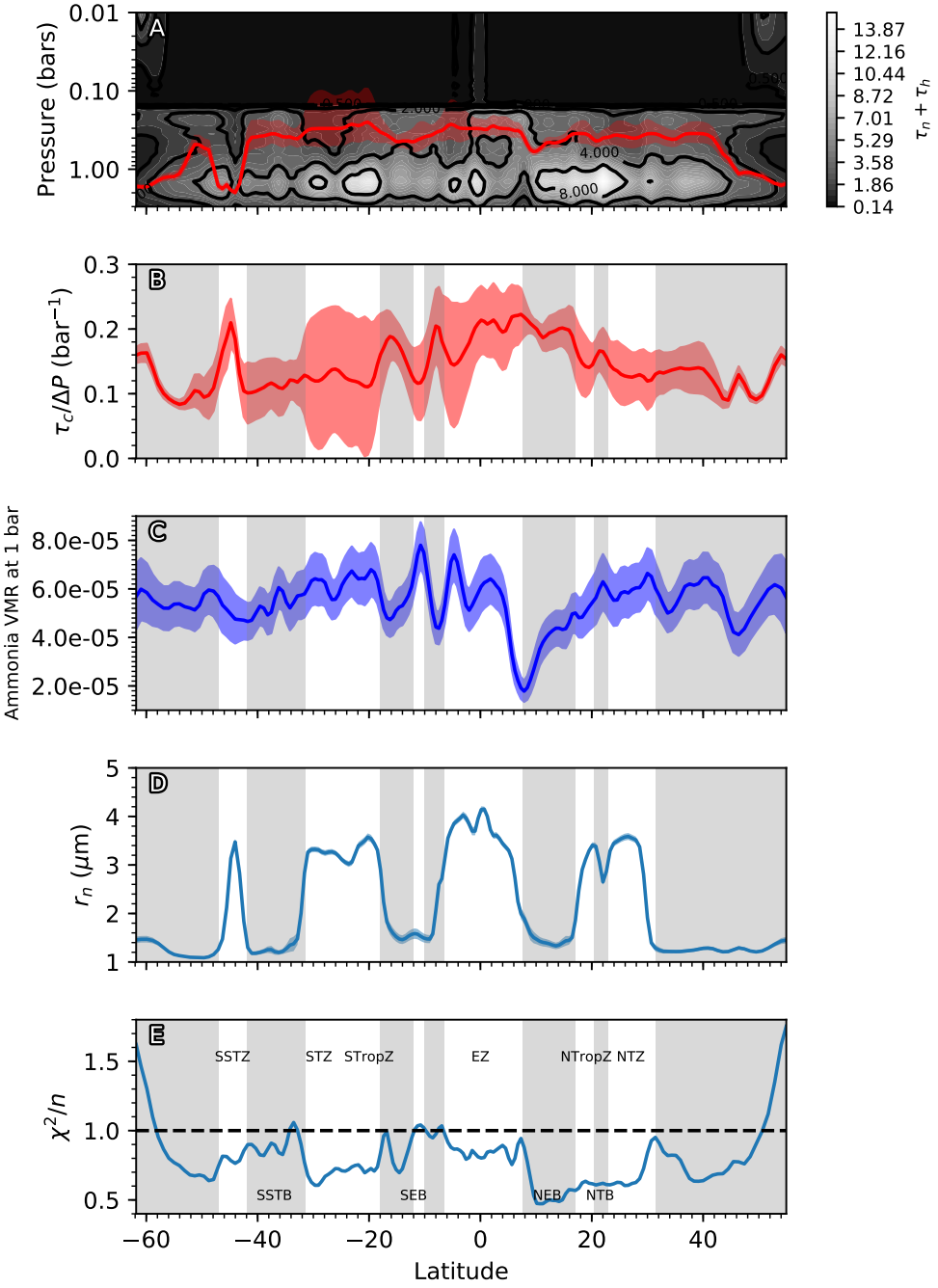


**Figure 13:** Results of the retrieval of variations in cloud, haze, colour and ammonia gas over the swath of Jupiter shown in Figure 6, as a function of planetocentric latitude. Gaussian smoothing over latitude was performed for these plots in order to remove pixel-to-pixel fluctuations in the retrieved parameters and instead observe general trends. Plot A shows the vertical profile of cloud ($\tau_n/\Delta p$, $P > 0.15$ bars) and haze ($\tau_h/\Delta p$, $P < 0.15$ bars) abundance in units of optical depth/bar, with iso-contours at 0.5, 1, 2, 4 and 8 bar$^{-1}$ respectively. In red is shown the retrieved chromophore altitude $P_c$. Plot B shows the retrieved chromophore abundance $\tau_c/\Delta p$, also in units of optical depth/bar, with errors shaded in light red. Plot C shows the retrieved gaseous ammonia profile sampled at 1 bar, approximately the level of greatest sensitivity to ammonia gas based on the retrieved pressure levels of the cloud layers, with uncertainties shaded in light blue. Plot D shows the retrieved cloud particle effective radius $r_n$ in μm. Finally, Plot E shows the goodness of fit ($\chi^2/n$) to the spectrum at each latitude. The approximate boundaries between the zones (in white) and belts (in grey) are marked in plots B-E, with the names of the respective zones and belts marked in plot E.

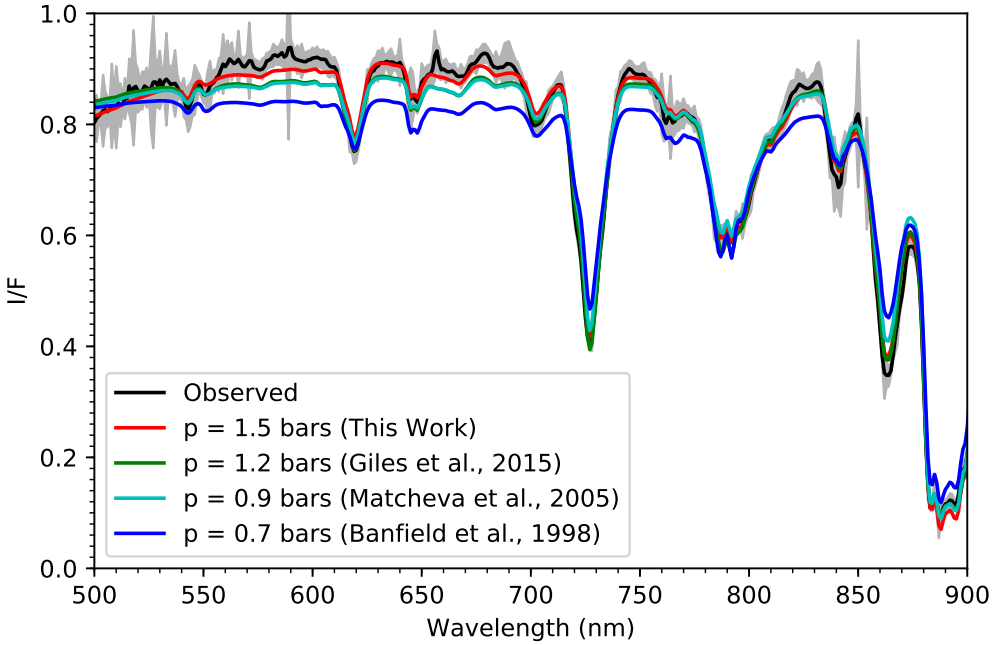


**Figure 14:** Spectral fit to the EZ (lat, lon = 2.86$^o$, 5.16$^o$) when $\tau_n$ is set to fall to 0 deeper than four different pressure levels as stated in the legend, in order to simulate the base level of the deepest visible cloud layer as found by Banfield et al. (1998) from Galileo/SSI data in the near-IR, Matcheva et al. (2005) from Cassini/CIRS observations in the mid-IR, and Giles et al. (2015) from Cassini/VIMS-IR data at 5 μm. We find that the best fit to the EZ is provided when the deepest visible cloud layer is located around 1.5 bars ($\chi^2/n$ = 1.31), while placing the cloud base at 1.2 bars ($\chi^2/n$ = 2.67), 0.9 bars ($\chi^2/n$ = 3.94) or especially at 0.7 bars ($\chi^2/n$ = 11.1) underestimates I/F at visible continuum wavelengths relative to wavelengths of major methane absorption. The reader should note that the Giles et al. (2015) and Matcheva et al. (2005) retrievals match very closely, except at the 860 nm methane absorption feature.